

Optical Bragg, atom Bragg and cavity QED detections of quantum phases and excitation spectra of ultracold atoms in bipartite and frustrated optical lattices

Jinwu Ye ^{1,5}, Yan Chen ², J.M. Zhang ³, W.M. Liu ³, K.Y. Zhang ⁴, Yan Li⁴, W.P. Zhang ⁴ and C.L. Zhang ⁵

¹ Department of Physics and Astronomy, Mississippi State University, P. O. Box 5167, Mississippi State, MS, 39762

² Department of Physics, Surface Physics Laboratory (National Key Laboratory) and Lab of Advanced Materials, Fudan University, Shanghai, China

³ Institute of Physics, Chinese Academy of Sciences, Beijing, 100080, China

⁴ Department of Physics, East China Normal university, Shanghai, 200062, China

⁵ Beijing Key Laboratory for Terahertz Spectroscopy and Imaging,

Key Laboratory of Terahertz Optoelectronics, Ministry of Education,

Department of Physics, Capital Normal University, Beijing, 100048 China

(Dated: January 22, 2019)

Ultracold atoms loaded on optical lattices can provide unprecedented experimental systems for the quantum simulations and manipulations of many quantum phases and quantum phase transitions between these phases. However, so far, how to detect these quantum phases and phase transitions effectively remains an outstanding challenge. In this paper, we will develop a systematic and unified theory of using the optical Bragg scattering, atomic Bragg scattering or cavity QED to detect the ground state and the excitation spectrum of many quantum phases of interacting bosons loaded in bipartite and frustrated optical lattices. We show that the two photon Raman transition processes in the three detection methods not only couple to the density order parameter, but also the *valence bond order* parameter due to the hopping of the bosons on the lattice. This valence bond order coupling is very sensitive to any superfluid order or any Valence bond (VB) order in the quantum phases to be probed. These quantum phases include not only the well known superfluid and Mott insulating phases, but also other important phases such as various kinds of charge density waves (CDW), valence bond solids (VBS), CDW-VBS phases with both CDW and VBS orders unique to frustrated lattices, various kinds of supersolids and quantum phase transitions between these phases. We analyze respectively the experimental conditions of the three detection methods to probe these various quantum phases and their corresponding excitation spectra. We also contrast the three experiments and discuss their strengths and weaknesses in detecting all these quantum phases. The effects of a finite temperature and a harmonic trap are also addressed.

I. INTRODUCTION

Various kinds of strongly correlated quantum phases of matter may have wide applications in quantum information processing, storage and communications¹. It was widely believed and also partially established that due to the tremendous tunability of all the parameters in this system, ultracold atoms loaded on optical lattices (OL) can provide an unprecedented experimental systems for the quantum simulations and manipulations of these quantum phases and quantum phase transitions between these phases. For example, Mott and superfluid phases³ may have been successfully simulated and manipulated by ultra-cold atoms loaded in a cubic optical lattice⁴. However, there are still at least two outstanding problems remaining. The first is to how to realize many important quantum phases¹. The second is that assuming the favorable conditions to realize these quantum phases are indeed achieved in experiments, how to detect them without ambiguities. In this paper, we will address the second question.

Because these ultra-cold atoms are charge neutral, so in contrast to many condensed matter systems, they can not be manipulated electrically or magnetically, so the experimental ways to detect these quantum phases of cold atoms are rather limited. The earliest detection method is through the so called time of flight

measurement^{1,4} which simply opens the trap and turn off the optical lattice and let the trapped atoms expand and interfere, then take the image. This kind of measurement is destructive and may not be used to detect the ground state and excitation spectrum of quantum phases in optical lattices. There are also other detection methods such as the Optical Bragg scattering in Fig.1a and the atom Bragg scattering in Fig.1b. The Optical Bragg scattering (Fig.1a) has been used previously to study periodic lattice structures of cold atoms loaded on optical lattices⁷. It was also proposed as an effective method for the thermometry of fermions in an optical lattice⁸. Recently, it was argued that it can be used to detect the putative anti-ferromagnetic ground state of fermions in OL⁹. There are also very recent optical Bragg scattering experimental data from a Mott state, a BEC and some artificial AF state¹⁰. The atom Bragg diffraction in Fig.1b (also called "atom Bragg spectroscopy") is based on stimulated matter waves scattering by two incident laser pulses^{5,6}, then take images through the time of flight measurements. There are also two kinds of "atom Bragg spectroscopies". The momentum⁵ transfer Bragg spectroscopy was used to detect the Bogoliubov mode inside an BEC condensate. The energy transfer⁶ Bragg spectroscopy was used to detect the Mott gap in a Mott state in an optical lattice. The photon and atom Bragg diffractions are two complementary experimental detection

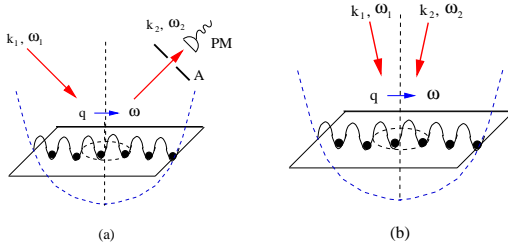


FIG. 1: Optical (a) and atom (b) Bragg scattering of cold atoms moving in 2 dimensional optical lattices. The $\vec{q} = \vec{k}_1 - \vec{k}_2$ and $\omega = \omega_1 - \omega_2$ are momentum and energy transfer from the laser beams to the cold atoms respectively. Tilting and rotating the incident beam(s) around the dashed line can probe the ground state and the excitation spectrum of the whole 2d optical lattice.

tion methods. During the last several years, there have been extensive of experimental and theoretical research combining cavity QED and cold atoms. For example, several experiments^{11,12} successfully achieved the strong coupling of a BEC of $N \sim 10^5$ ^{87}Rb atoms to the photons inside an ultrahigh-finesse optical cavity. The superradiant phase²¹ was realized in a recent experiments¹⁹ using BEC and also in a previous experiment using thermal atoms²⁰ where the effective two "atomic" levels are the two momentum states of the cold atoms in the optical lattice formed by the cavity field and the off-resonant transverse pumping Laser. Since the first experimental observation of the bi-stabilities of BEC atoms at very low photon numbers inside a cavity¹³, there have been very active theoretical studies on the bi- or multi-instabilities of BEC spinors¹⁴, spinless fermions¹⁵ or BEC with a spin-orbit coupling¹⁶ inside a cavity. It was also proposed that the cavity photons may be used to non-destructively detect superfluid and Mott phases of ultra-cold atoms in optical lattices^{17,18}.

In this paper, we will explore the applicabilities of both photon Bragg diffraction and atom Bragg diffraction to detect several important quantum phases in both bipartite and frustrated lattices. We will also discuss in detail the possibility that the cavity QED can be used as a possible new detection method. We will develop a systematic and unified theory of using the optical Bragg scattering, atomic Bragg scattering or cavity QED to detect the nature of quantum phases such as both the ground state and the excitation spectrum above the ground state of interacting bosons loaded in optical lattices.

The Extended Boson Hubbard Model (EBHM) with various kinds of interactions, on all kinds of lattices and at different filling factors is described by the following Hamiltonian^{2-4,22,23,25-31}:

$$H_{BH} = -t \sum_{\langle ij \rangle} (b_i^\dagger b_j + h.c.) - \mu \sum_i n_i + \frac{U}{2} \sum_i n_i(n_i - 1) + V_1 \sum_{\langle ij \rangle} n_i n_j + V_2 \sum_{\langle ik \rangle} n_i n_k + \dots \quad (1)$$

where $n_i = b_i^\dagger b_i$ is the boson density, t is the nearest neighbor hopping which can be tuned by the depth of the optical lattice potential, the U, V_1, V_2 are onsite, nearest neighbor (nn) and next nearest neighbor (nnn) interactions respectively, the \dots may include further neighbor interactions and possible ring-exchange interactions. The filling factor $n = N_a/N$ where N_a is the number of atoms and N is the number of lattice sites. The on-site interaction U can be tuned by the Feshbach resonance³. There are many possible ways to generate longer range interaction V_1, V_2, \dots of ultra-cold atoms loaded in optical lattices. Being magnetically or electrically polarized, the ^{52}Cr atoms³⁶ or polar molecules³⁷⁻⁴⁰ $^{40}\text{K} + ^{87}\text{Rb}$ (or $^{39}\text{K} + ^{87}\text{Rb}$) interact with each other via long-rang anisotropic dipole-dipole interactions. Loading the ^{52}Cr or the polar molecules on a 2d optical lattice with the dipole moments perpendicular to the trapping plane can be mapped to Eqn.1 with long-range repulsive interactions $\sim p^2/r^3$ where p is the dipole moment. The CDW supersolid phases studied by QMC²³ and described in²⁹ by the dual vortex method was numerically found to be stable in large parameter regimes in this system³⁸. Possible techniques to generate long-range interactions in a gas of groundstate alkali atoms by weakly admixing excited Rydberg states with laser light was proposed in³⁹. The generation of the ring exchange interaction has been discussed in⁴⁰.

Various kinds of bipartite and frustrated optical lattices can be realized by suitably choosing the geometry of the laser beams forming the optical lattices. For example, using three coplanar beams of equal intensity having the three vectors making a 120° angle with each other, the potential wells have their minima in a honeycomb or a triangular lattice³⁴. Four beams travel along the three fold symmetry axes of a regular tetrahedron, the potential wells have their minima in a body-centered-cubic lattice³⁴. The authors in³⁵ proposed to create a kagome optical lattice using superlattice techniques. It was known that cold atoms in a frustrated lattice show completely different behaviors than in a bipartite lattice. Some of the important phases with long range interactions in both bipartite and frustrated lattices are studied in detail in^{29,30} and briefly reviewed in the Sec.II.

In this paper, we explicitly show that the two photon Raman transition processes shown in Fig.6 in the optical Bragg scattering, atomic Bragg scattering or cavity QED (with the scattered light replaced by the cavity photon in Fig.14) not only couple to the density order parameter, but also the valence bond order parameter due to the hopping of the bosons on the lattice. This kinetic energy coupling is extremely sensitive to any superfluid order or any Valence bond (VB) order which can be considered as a local superfluid order on a local bond at corresponding ordering wavevectors. By tuning the incident angle in the Fig.1a, the angle between the two laser lights in Fig.1b or the incident light and the cavity axis in Fig.14a, one can detect both the ground state and the excitation spectrum by measuring the light scattering cross sections,

the scattered clouds or leaking cavity photon numbers respectively. The static structure function can detect not only the well known superfluid and Mott insulating phases, but also other interesting phases such as charge density wave (CDW), both dimer and plaquette valence bond solids (VBS), even some CDW-VBS phase unique in frustrated lattices at commensurate fillings^{22,23,26–31}. It can also detect the corresponding CDW supersolids and VB supersolids at in-commensurate fillings in both bipartite and frustrated lattices. Furthermore, the dynamic structure function can detect the excitation spectrum and the corresponding spectral weights in all these quantum phases.

The rest of the paper is organized as the follows. In Sec.II, we will review several important phases in both bipartite and frustrated lattices. We also stress a recently discovered new phase which has both CDW and VBS order called CDW-VBS phase in the triangular lattice. This kind of CDW-VBS phase is unique and quite common to frustrated lattices. In Sec.III, just from symmetry breaking points of view, we study several very general and important properties of density-density, bond-bond correlation functions and their finite size scaling properties inside a flat trap⁴². In Sec. IV, we study the off-resonant light scattering from the two level atoms hopping in an optical lattice and find the off-resonant light beams not only couple to the density, but also the kinetic energy of the cold atoms hopping on a optical lattice. We also estimate the relative strengths of the two couplings by using the harmonic approximation³. We show that the light scattering cross section is the sum of the density-density and bond-bond correlation function with the corresponding form factors. In Sec.V, we study the density-density correlation function in the superfluid, Mott and quantum critical regime at integer filling case from both the boson action and its dual vortex action. All the previous work seem focused on the order parameter correlation functions instead of the density-density ones which are measured by the the three experimental detection methods. In Sec. VI, we study the elastic scattering cross section in a CDW to detect the ground state, also in-elastic scattering cross section to detect the excitation spectrum and its scaling form near the second order transition from the CDW and CDW supersolid. In Sec. VI, we study the elastic scattering cross section in a VBS to detect the ground state, also in-elastic scattering cross section to detect its excitation spectrum and its scaling form near the second order transition from the VBS and VBS supersolid. In Sec. VII, we extend our discussions to frustrated lattices and stress several new features in the density-density and bond-bond correlation functions unique to frustrated lattices. Then we apply the formalism to study the light scattering cross sections from the X-CDW, VBS and CDW-VBS phases in a triangular lattice. We discuss light Bragg scattering experiment and a possible quantum beat measurement in Sec. VIII, both momentum and energy atom Bragg scattering experiments in Sec.IX. In Sec. X, we pro-

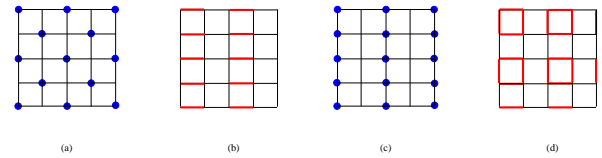


FIG. 2: Several insulating states at filling factor $f = 1/2$ in a square lattice. (a) The charge density wave (CDW) phase with ordering wavevector $\vec{Q}_n = (\pi, \pi)$. (b) valence bond solid (VBS) phases with ordering wavevector $\vec{Q}_K = (\pi, 0)$ where the kinetic energy $\langle K_{ij} \rangle = \langle b_i^\dagger b_j + h.c. \rangle$ takes a non-zero constant K in the two sites connected with a dimer, but 0 in the two sites without a dimer. (c) Stripe CDW order at $\vec{Q}_n = (\pi, 0)$ and (d) Plaquette VBS order at $\vec{Q}_{K1} = (\pi, 0), \vec{Q}_{K2} = (0, \pi)$. See Refs.^{22,27–30}.

pose to use cavity QED as an effective detection method. Phase sensitive homodyne measurement and the Fluorescence spectrum measurement can be used to detect the ground state and excitation spectrum of various quantum phases. This possible cavity enhanced off-resonant light scattering detection method should be complementary to the light scattering and atom Bragg scattering discussed in the previous sections. We contrast the three experiments, discuss their strengths and weaknesses in detecting all these quantum phases and summarize our results in Sec.XI. In the appendix A, we point out some mistakes in the previous work¹⁷ and show that the light scattering cross section or cavity QED scattering at the classical diffraction minimum $\vec{q} = (\pi, \pi)$ may be an effective measurement of the superfluid density. In the appendix B, we point out the possibility to experimentally observe a stable ring-structure supersolid inside a harmonic trap. In the following, we just take 2d optical lattices as examples. The 1d and 3d cases can be similarly discussed. A short report on some results of this paper already appeared in⁴¹.

II. REVIEW OF QUANTUM PHASES IN BIPARTITE AND FRUSTRATED LATTICES

Quantum phases of the Extended Boson Hubbard Model (EBHM) with long range interactions in Eqn.1 are thoroughly studied by various analytic and numerical methods such as the spin wave expansion in Ref.²², the dual vortex method in Refs.^{27–30} and quantum Monte-Carlo simulations in Refs.^{23,24,26,31}. Some of the important Mott insulating phases at commensurate fillings in a square lattice are summarized in the Fig.2. In the following, we review some interesting quantum phases in bipartite and frustrated lattices respectively. This section is not new, but pave the way for the discussions in the following sections on the detection methods of these quantum phases.

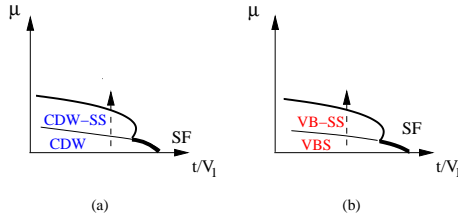


FIG. 3: Zero temperature Phase diagram of the boson Hubbard model with nearest neighbor interaction V_1 near half filling in a bipartite lattice²⁹. The labels of the axes are given in Eqn.1. (a) Ising limit. (b) Easy-Plane limit. See also Fig. 11 for the finite temperature phase diagram and Fig.16 for the phases inside a trap.

A. Some Quantum phases in bipartite optical lattices

Some quantum phases, especially supersolid phases and quantum phase transitions slightly away from commensurate fillings are also studied by these methods. The CDW supersolid phases studied by QMC in Ref.^{23,24,31} and described in Ref.²⁹ by the dual vortex method were numerically found to be stable in large parameter regimes in the dipolar systems in Ref.³⁸. The zero temperature phase diagrams of the chemical potential μ against the quantum fluctuations t/V_1 slightly away from $1/2$ fillings are shown in the Fig.3.

In Eqn.33, we will show that the Bragg spectroscopy couples to both the density-density and bond-bond correlation function with the strength $\sim |f_0|^2$ and $\sim |f_x|^2$ respectively.

In a honeycomb lattice, we can also find some CDW and VBS phases^{29,30}. Because of their similarity to the quantum phases in a square lattice, we will not discuss the honeycomb lattice specifically.

B. Some Quantum phases in frustrated optical lattices

In a triangular lattice at the filling factor $f = 1/3$, it is easy to see a CDW phase and a triangular Valence bond (TVB) phase³⁰.

The density in the X-CDW Fig.4a is:

$$\rho(\vec{r}) = A \cos \vec{Q}_n \cdot \vec{r} + 1/3 \quad (2)$$

where $\vec{Q}_n = 2\pi/3(1, 1)$. If $\vec{Q}_n = 2\pi/3(1, 0)$, then Eqn.2 stands for a stripe phase along \vec{a}_1 .

The triangular VB state in Fig.4b is:

$$\begin{aligned} B_1(\vec{r}) &= K_1 \cos \vec{Q}_K \cdot \vec{r} + K_2 \\ B_d(\vec{r}) &= K_1 \cos \vec{Q}_K \cdot \vec{r} + K_2 \\ B_2(\vec{r}) &= K_1 \cos(\vec{Q}_K \cdot \vec{r} - \frac{2\pi}{3}) + K_2 \end{aligned} \quad (3)$$

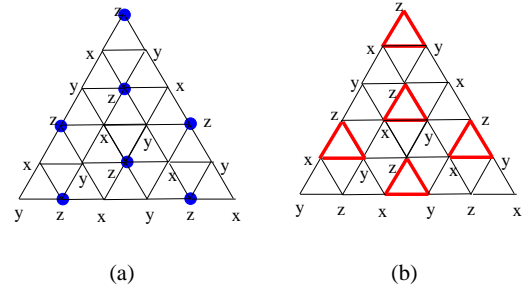


FIG. 4: Several insulating states at filling factor $f = 1/3$ in a triangular lattice (a) the X-CDW at $\vec{Q}_n = 2\pi/3(1, 1)$ (b) VBS at $\vec{Q}_K = 2\pi/3(1, 1)$. See^{22,30}.

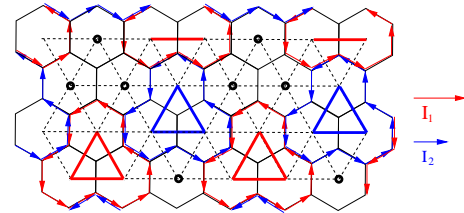


FIG. 5: The CDW-VB phase in a triangular lattice at $f = 1/3$ in the easy plane limit $v < 0, w > 0$. The $(0, 0)$ sets the origin of the direct triangular lattice. There are two different vortex currents flowing in the dual honeycomb lattice. The red current is $I_1 = \sin \frac{3\pi}{9} + \sin \frac{2\pi}{9}$, the blue current $I_2 = \sin \frac{\pi}{9} + \sin \frac{2\pi}{9}$. The two different currents indicate 3 boson different densities in the direct triangular lattice. The density and bond distributions are given in Eqn.4 and Eqn.5 respectively. See³⁰.

where $\vec{Q}_K = 2\pi/3(1, 1)$ and the $B_1(\vec{r}), B_d(\vec{r}), B_2(\vec{r})$ are the three bonds along the 3 directions along $\vec{a}_1, \vec{a}_d, \vec{a}_2$. One can see that $B_2(\vec{r}) = B_1(\vec{r} - \vec{a}_1)$ as expected from the symmetry breaking patterns in Fig.4b.

In a triangular lattice, we also identify a phase with both CDW and VBS order in Fig.5³⁰. The CDW order in the CDW+VBS phase is given by:

$$\begin{aligned} \rho_{CV}(\vec{x}) &= 1/3 + 4\delta \sqrt{\frac{I_1^2 - I_1 I_2 + I_2^2}{3}} [-\cos(\frac{2\pi}{3}x + \frac{5\pi}{18}) \\ &+ \cos(\frac{2\pi}{3}y + \frac{\pi}{18}) + \cos(\frac{2\pi}{3}(x - y) + \frac{\pi}{18})] \end{aligned} \quad (4)$$

where δ is the CDW order parameter and I_1, I_2 are the vortex currents in Fig.5.

The VBS order in the CDW+VBS phase is given by:

$$\begin{aligned}
B_1(\vec{x}) &= B_d(\vec{x}) = c\delta(I_1 + I_2)(1 + 2\cos\frac{2\pi}{3}(x+y)) \\
&+ 2c\delta\sqrt{I_1^2 - I_1I_2 + I_2^2}[\cos(\frac{2\pi}{3}x + \frac{2\pi}{9}) \\
&+ \cos(\frac{2\pi}{3}y - \frac{2\pi}{9}) + \cos(\frac{2\pi}{3}(x-y) - \frac{2\pi}{9})] \\
B_2(\vec{x}) &= c\delta(I_1 + I_2)(1 + 2\cos[\frac{2\pi}{3}(x+y) - \frac{2\pi}{3}]) \\
&+ 2c\delta\sqrt{I_1^2 - I_1I_2 + I_2^2}[\cos(\frac{2\pi}{3}x - \frac{4\pi}{9}) \\
&+ \cos(\frac{2\pi}{3}y - \frac{2\pi}{9}) + \cos(\frac{2\pi}{3}(x-y) - \frac{8\pi}{9})] \quad (5)
\end{aligned}$$

where the c is an unknown constant. One can see that $B_2(\vec{x}) = B_1(\vec{x} - \vec{a}_1)$ as expected from the symmetry breaking patterns in Fig.5.

When comparing with the CDW order in Eqn.4, we can see that in addition to the 3 ordering wave vectors $\vec{Q}_\alpha = 2\pi/3(1,0), 2\pi/3(0,1), 2\pi/3(1,-1), \alpha = 1, 2, 3$, there is also a new VBS ordering wave vector $\vec{Q}_4 = 2\pi/3(1,1)$. It is this new ordering wave vector which makes the detection of the VBS order inside the CDW-VB phase possible to be discussed in Sec.VIII.

In a Kagome lattice, we also found some interesting CDW, VBS and CDW+VBS phase³⁰. Because of their similarity to the quantum phases in a triangular lattice, we will not discuss the Kagome lattice specifically.

III. DENSITY-DENSITY AND BOND-BOND CORRELATION FUNCTIONS

In this section, from symmetry breaking point of view, we will study several important properties of the density-density correlation functions and the bond-bond correlation functions in these quantum phases in a bipartite lattice respectively. The counterparts in a frustrated lattice will be discussed in Sec.VIII. The results achieved should also be useful to Quantum Monte Carlo simulations^{23,24,31} on the extended boson Hubbard model in Eqn.1 in a finite $N = L \times L$ lattice.

A. Density-Density correlation function

One can write the density at site i as

$$N_i = n_i + (-1)^i m_i \quad (6)$$

where $i = x$ for the $(\pi, 0)$ stripe CDW in Fig.2c and $i = x+y$ for the (π, π) CDW in Fig.2c. Then the density-density correlation function in Eqn.33 is defined as:

$$S_N(\vec{q}, t) = \frac{1}{N^2} \sum_{i,j} e^{-i\vec{q} \cdot (\vec{r}_i - \vec{r}_j)} \langle N_i(t) N_j(0) \rangle \quad (7)$$

By substituting the decomposition of N_i into the above Eqn. we can get:

$$\begin{aligned}
S_N(\vec{q}, t) &= \frac{1}{N} \sum_i e^{-i\vec{q} \cdot \vec{r}_i} \langle n(i, t) n(0, 0) \rangle_C + n^2 \delta_{\vec{q}, 0} \\
&+ \frac{1}{N} \sum_i e^{-i(\vec{q} - \vec{Q}_N) \cdot \vec{r}_i} \langle m(i, t) m(0, 0) \rangle_C \\
&+ m^2 \delta_{\vec{q}, \vec{Q}_N} \quad (8)
\end{aligned}$$

where we have used the translational invariance to get rid of one summation, $\langle n_i(t) n_j(0) \rangle_C = \langle n_i(t) n_j(0) \rangle - n^2$ and $\langle m_i(t) m_j(0) \rangle_C = \langle m_i(t) m_j(0) \rangle - m^2$ are connected Green functions.

Its Fourier transform leads to the dynamic structure function:

$$\begin{aligned}
S_N(\vec{q}, \omega) &= \int dt e^{-i\omega t} S_N(\vec{q}, t) \\
&= n^2 \delta_{\vec{q}, 0} \delta(\omega) + \frac{1}{N} S_n^{inel}(\vec{q}, \omega) \\
&+ m^2 \delta_{\vec{q}, \vec{Q}_N} \delta(\omega) + \frac{1}{N} S_m^{inel}(\vec{q}, \omega) \quad (9)
\end{aligned}$$

where the first and the third $\delta(\omega)$ terms denote the elastic scattering at $\vec{q} = 0$ and $\vec{q} = \vec{Q}_N$ respectively $S_n^{el} \delta(\omega) = n^2 \delta_{\vec{q}, 0} \delta(\omega)$, $S_m^{el} \delta(\omega) = m^2 \delta_{\vec{q}, \vec{Q}_N} \delta(\omega)$, the second and the fourth terms denote the inelastic scattering near $\vec{q} = 0$ and $\vec{q} = \vec{Q}_N$ respectively.

The equal time density-density correlation function is:

$$\begin{aligned}
S_N(\vec{q}, t=0) &= \frac{1}{N} \sum_i e^{-i\vec{q} \cdot \vec{r}_i} \langle n(i, 0) n(0, 0) \rangle_C + n^2 \delta_{\vec{q}, 0} \\
&+ \frac{1}{N} \sum_i e^{-i(\vec{q} - \vec{Q}_N) \cdot \vec{r}_i} \langle m(i, 0) m(0, 0) \rangle_C \\
&+ m^2 \delta_{\vec{q}, \vec{Q}_N} \quad (10)
\end{aligned}$$

From $S_N(\vec{q}, t=0) = \int \frac{d\omega}{2\pi} S_N(\vec{q}, \omega)$, we can write the equal-time correlation function as the sum of the elastic one and the in-elastic one:

$$S_N(\vec{q}, t=0) = S_n^{el} + \frac{1}{N} S_n^{inel}(\vec{q}) + S_m^{el} + \frac{1}{N} S_m^{inel}(\vec{q}) \quad (11)$$

where $S_n^{el} = n^2 \delta_{\vec{q}, 0}$, $S_m^{el} = m^2 \delta_{\vec{q}, \vec{Q}_N}$ and $S_n^{inel}(\vec{q}) = \int \frac{d\omega}{2\pi} S_n^{inel}(\vec{q}, \omega)$, $S_m^{inel}(\vec{q}) = \int \frac{d\omega}{2\pi} S_m^{inel}(\vec{q}, \omega)$.

In the following, we discuss the density-density correlation functions in the superfluid, CDW and CDW supersolid respectively.

(a) Superfluid state near the CDW state

In the superfluid state, the first term in Eqn.8 stands for the gapless superfluid mode near $\vec{q} = 0$. Taking the results from Ref.^{43,44}, we have:

$$S_n(\vec{q}, \omega) = \langle \delta n(-\vec{q}, -\omega_n) \delta n(\vec{q}, \omega_n) \rangle = \frac{\rho_s q^2}{\omega_n^2 + v^2 q^2} \quad (12)$$

where $v^2 = \rho_s/\kappa$ is the superfluid phonon velocity, the ρ_s is the superfluid density and the κ is the compressibility.

Indeed $\kappa = S_n(\vec{q} \rightarrow 0, \omega = 0)$ as it should be. From the analytical continuation $i\omega_n \rightarrow \omega + i\delta$ and taking the imaginary part, we can identify the dynamic structure factor:

$$S_n^>(\vec{q}, \omega) = S_n(q)\delta(\omega - vq), \quad S_n(q) = \rho_s q \pi / 2v \quad (13)$$

where the $S_n(q)$ is the equal time density-density correlation function near $q = 0$ shown in Fig.10a1.

The second term near $\vec{q} = \vec{Q}_N$ in Eqn.8 comes from the roton contribution near $\vec{q} = \vec{Q}_N$ in Fig.10a1. The dispersion near $\vec{q} = \vec{Q}_N$ can be taken as $\omega(q) \sim \Delta_r + \frac{2m_r}{(\vec{q} - \vec{Q}_N)^2}$ where $\Delta_r > 0$ is the roton gap. There is no CDW order yet, so $m = 0$ in the Eqn.8. However, as one approaches the CDW from the SF in Fig.3a, there is a first order transition into the CDW driven by the collapse of the roton gap Δ_r .

(b) *CDW state*

In the CDW state, the nn correlator near $\vec{q} = 0$ in Eqn.8 is very small, so can be dropped safely, so one only need to focus on the mm correlator near $\vec{q} = \vec{Q}_N$. The discrete lattice symmetry was broken due to the non-uniform density distribution, so $m \neq 0$, there is also a gap Δ_{CDW} in the CDW state, so the connected equal time correlation function decays exponentially in the CDW state:

$$\langle m_i(0)m_j(0) \rangle_C \sim e^{-|\vec{r}_i - \vec{r}_j|/\xi_{CDW}} \quad (14)$$

where $\xi_{CDW} \sim 1/\Delta_{CDW}$ is the correlation length in the CDW. So the fluctuation part in Eqn.10 is only at the order of $\sim 1/N$, we conclude:

$$S_N(\vec{Q}_N, t = 0) = m^2 + \frac{1}{N} S_m^{inel}(\vec{q} = \vec{Q}_N) = m^2 + O(1/N) \quad (15)$$

Here we can see that the equal time structure factor is the sum of the elastic scattering $S_m^{el} = m^2$ plus a $1/N$ in-elastic background.

For $\vec{q} \neq \vec{Q}_N$, but close to \vec{Q}_N , then we find

$$S_N(\vec{q}, t) \sim \frac{1}{N} \sum_i e^{-i(\vec{q} - \vec{Q}_N) \cdot \vec{r}_i} \langle m(i, t)m(0, 0) \rangle_C \quad (16)$$

where one can extract the excitation spectrum and spectral weight of the CDW near $\vec{q} \neq \vec{Q}_N$ shown in Fig.10c1. In fact, the excitation spectrum around $\vec{k} - \vec{Q}_N = \vec{q}$ can also be extracted from the Feynman relation:

$$\omega_{CDW}(\vec{q}) = \frac{\int_{-\infty}^{\infty} d\omega \omega S_N(\vec{q}, \omega)}{\int_{-\infty}^{\infty} d\omega S_N(\vec{q}, \omega)} \quad (17)$$

which holds at $\vec{q} \rightarrow 0$, but not at $\vec{q} = 0$. The f -sum rule $\int_{-\infty}^{\infty} d\omega \omega S_N(\vec{q}, \omega) = \langle [[n(\vec{q}), H], n(-\vec{q})] \rangle$ at $d = 2$ gives:

$$\begin{aligned} \int_{-\infty}^{\infty} d\omega \omega S_N(\vec{q}, \omega) &= -2t \sum_{\vec{k}} [(\cos q_x - 1) \cos k_x \\ &+ (\cos q_y - 1) \cos k_y] \langle \Psi_0 | b_{\vec{k}}^\dagger b_{\vec{k}} | \Psi_0 \rangle \end{aligned} \quad (18)$$

where the $|\Psi_0\rangle$ is the ground state.

The $d = 1$ version of this sum rule was used to extract the excitation spectra by QMC in both the SF and the CDW state in Ref.²⁵. Note that at $d = 1$, the SF to the CDW transition in Fig.3a is in the Kosterlitz-Thouless (KT) transition universality class instead of first order transition in $d = 2$ and $d = 3$. It was shown in²⁹ that the CDW to the CDW SS transition at $d = 2$ along the vertical axis is in the same universality class of SF to Mott transition with the critical exponents $z = 2, \nu = 1/2, \eta = 0$. This was indeed confirmed by QMC in²⁵. It has no logarithmic correction at $d = 1$, in contrast to the logarithmic correction at $d = 2$ which is at the upper critical dimension²⁹. We expect that the SF to the CDW-SS transition is also in the KT transition universality class.

(c) *CDW Supersolid state*

In this case, the first term near $\vec{q} = 0$ in Eqn.8 stands for the gapless superfluid mode as given by Eqn.12 and shown in the lower branch in Fig.10b1.

The static order at $\vec{q} = \vec{Q}_N$ is given by Eqn.15 and the dynamic structure factor close to \vec{Q}_N in the upper branch in Fig.10b1 is given by Eqn.16 respectively.

B. The bond-bond correlation function

In a VBS or a VBS superfluid state, the density is *uniform*, then the Eqn.8 should be replaced by:

$$S_N(\vec{q}, t) = \frac{1}{N} \sum_i e^{-i\vec{q} \cdot \vec{r}_i} \langle n(i, t)n(0, 0) \rangle_C + n^2 \delta_{\vec{q}, 0} \quad (19)$$

where there is no staggered component m .

Inside a VBS state with a ordering wavevector \vec{Q}_K , there is a big CDW gap in the connected density-density correlation function in Eqn.19. Obviously, this CDW gap is much larger than the VBS gap introduced below Eqn.22. Furthermore, $S_N(\vec{Q}_K, 0) = \frac{1}{N} \sum_i e^{-i\vec{Q}_K \cdot \vec{r}_i} \langle n(i, 0)n(0, 0) \rangle_C$ is a smearing of a very small density fluctuation on a lattice scale, so it contributes to a very small background which is completely negligible compared to the VBS fluctuations near \vec{Q}_K to be discussed in the following. However, inside a superfluid, it may still be appreciable even at the classical diffraction minimum $\vec{q} = (\pi, \pi)$ as shown in the appendix A.

(a) *Superfluid near the VBS state*

The gapless superfluid mode near $\vec{q} = 0$ in Eqn.19 is still given by Eqn.12, but there is no peak near $\vec{q} = \vec{Q}_K$ in Eqn.19. Instead, there is a peak near $\vec{q} = \vec{Q}_K$ in the bond-bond correlation function in Eqn.21. The excitation spectrum near $\vec{q} = \vec{Q}_K$ can be taken as $\omega_v(q) \sim \Delta_{rv} + \frac{(\vec{q} - \vec{Q}_K)^2}{2m_{rv}}$ where $\Delta_{rv} > 0$ is the " valence bond roton" gap. There is no VBS order yet, so $K = 0$ in the Eqn.21. However, as one approaches the VBS from the

SF in Fig.3b, there is a very weak first order transition into the VBS driven by the collapse of the gap Δ_{rv} .

(b) *VBS state*

The lattice symmetry was broken by the non-uniform kinetic energy, so $K \neq 0$. For the $\vec{Q}_K = (\pi, 0)$ VBS state, one can write the total kinetic energy strength between the site i and the site $i + \hat{x}$ as

$$\begin{aligned} D_{ix} &= B_{ix} + (-1)^{i_x} K_{ix} \\ D_{iy} &= B_{iy} = B_{ix} \end{aligned} \quad (20)$$

Then Eqn.8 need to be replaced by:

$$\begin{aligned} S_{K\alpha}(\vec{q}, t) &= \frac{1}{N} \sum_i e^{-i(\vec{q} - \vec{Q}_K) \cdot \vec{r}_i} \langle K_\alpha(i, t) K_\alpha(0, 0) \rangle_C \\ &+ K^2 \delta_{\vec{q}, \vec{Q}_K} \end{aligned} \quad (21)$$

where $\vec{Q}_K = (\pi, 0)$ is the ordering wavevector for the VBS and we neglected the very small BB fluctuations near $\vec{q} = 0$.

The equal time bond-bond correlation function is:

$$\begin{aligned} S_{K\alpha}(\vec{q}, t=0) &= \frac{1}{N} \sum_i e^{-i(\vec{q} - \vec{Q}_K) \cdot \vec{r}_i} \langle K_\alpha(i, 0) K_\alpha(0, 0) \rangle_C \\ &+ K^2 \delta_{\vec{q}, \vec{Q}_K} \end{aligned} \quad (22)$$

Inside the VBS, there is also a VBS gap Δ_{VBS} , so the connected equal time correlation function decays exponentially in the VBS state:

$$\langle K_{i\alpha}(0) K_{j\alpha}(0) \rangle_C \sim e^{-|\vec{r}_i - \vec{r}_j|/\xi_{VBS}} \quad (23)$$

where the $\xi_{VBS} \sim 1/\Delta_{VBS}$ is the correlation length in the VBS state. So the first term in Eqn.22 is at the order of $\sim 1/N$, so we conclude:

$$S_{K\alpha}(\vec{Q}_K, t=0) = K^2 + O(1/N) \quad (24)$$

For $\vec{q} \neq \vec{Q}_K$, but close to \vec{Q}_K , then one has

$$S_{K\alpha}(\vec{q}, t) \sim \frac{1}{N} \sum_i e^{-i(\vec{q} - \vec{Q}_K) \cdot \vec{r}_i} \langle K_\alpha(i, 0) K_\alpha(0, 0) \rangle_C \quad (25)$$

where one can extract the excitation spectrum and spectral weight of the VBS near $\vec{q} \neq \vec{Q}_K$ shown in Fig.10c2. The VBS excitation spectrum around $\vec{k} - \vec{Q}_K = \vec{q}$ can be extracted from the Feynman relation:

$$\omega_{K\alpha}(\vec{q}) = \frac{\int_{-\infty}^{\infty} d\omega \omega S_{K\alpha}(\vec{q}, \omega)}{\int_{-\infty}^{\infty} d\omega S_{K\alpha}(\vec{q}, \omega)} \quad (26)$$

which holds at $\vec{q} \rightarrow 0$, but not at $\vec{q} = 0$. The f -sum rule gives $\int_{-\infty}^{\infty} d\omega \omega S_{K\alpha}(\vec{q}, \omega) = \langle [[S_{K\alpha}(\vec{q}), H], S_{K\alpha}(-\vec{q})] \rangle$. Unfortunately, there is no simple expression for this double commutator which depends on the details of the Hamiltonian.

(c) *VBS supersolid state*

In this case, the gapless superfluid mode near $\vec{q} = 0$ Eqn.19 is still given by Eqn.12.

The static order at $\vec{q} = \vec{Q}_K$ is given by Eqn.24 and the dynamic structure factor close to \vec{Q}_K in the upper branch in Fig.10b2 is given by Eqn.25 respectively.

C. Finite size scaling of the correlation functions of ultra-cold atoms in a flat trap

Because the CDW (or VBS) and the SF break two completely different symmetries, so it is likely that there is a first order transition between them. Indeed, so far, any known transitions from CDW to SF in Fig.3a or from a VBS to a SF in Fig.3b are first order. However, if any of them is second order⁴⁸, then the density or the bond can be taken as the order parameters, the density-density or bond-bond correlation functions will diverge at the corresponding ordering wave vectors. In real cold atom experiments, any divergence in the density-density or bond-bond correlation functions in the thermodynamic limit will be cutoff by the trap size $L \sim 100\mu m$. With the optical lattice constant $a \sim 0.5\mu m$, the trap can hold around $N \sim 10^5 \sim 10^6$ number of particles. In fact, this size is already far bigger than the present largest quantum Monte-Carlo simulations. As shown in the appendix B, there are multiple phases inside an harmonic trap. Inside a flat trap⁴², a finite size scaling analysis can be used to extract the critical exponents. In a 2nd order transition with exponents z, ν, η , the finite size scaling form of the static and equal time density-density structure factor at the ordering wavevector \vec{Q} is:

$$\begin{aligned} S_n(\vec{Q}, i\omega_n = 0) &= L^{2-\eta} F_{ns}(L^{1/\nu}(K - K_c), \beta/L^z) \\ S_n(\vec{Q}, \tau = 0) &= L^{2-z-\eta} F_{ne}(L^{1/\nu}(K - K_c), \beta/L^z) \end{aligned} \quad (27)$$

where β is the inverse temperature, L is size of the system, K is the tuning parameter such as t/V_1 or μ in Fig.3. Similar quantities can be defined for bond-bond correlation functions $S_{K,\alpha}(\vec{k}, \tau = 0), S_{K,\alpha}(\vec{k}, i\omega_n = 0)$ where $K_{ij} = b_i^\dagger b_j + h.c.$ and $\alpha = \hat{x}, \hat{y}$ is the orientation of the bond $\langle ij \rangle$. In principle, by doing this finite size scaling with respect to the trap size L , finite temperature T , one can extract all the 3 exponents z, ν, η .

We will explicitly discuss the SF to Mott transition with the dynamic exponent $z = 1$ in Fig.8 in Sec. V, the CDW to CDW-SS and the VBS to VB-SS transition with $z = 2$ in Fig.11 in Sec. VI and VII respectively. Unfortunately, because the order parameter of these two quantum phase transitions are neither density nor the bond, so Eqn.27 do not apply. However, in view of the density is a conserved quantity, its scaling functions in the two transitions will be given in Eqn.50 and Eqn.56.

IV. TWO PHOTON RAMAN SCATTERING FORMALISMS.

In this section, we focus on the light scattering cross section in Fig.1a. As shown in Sec. X, it can be straightforwardly applied to the atom Bragg spectroscopy experiment in Fig.1b. As shown in Sect. XI, the cavity enhanced off-resonant scattering formalism is similar after we take care of the physics cavity specific to a cavity QED.

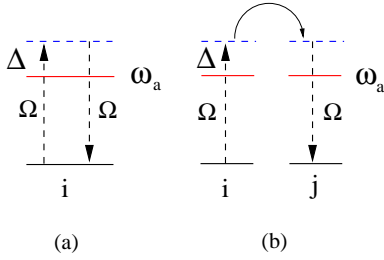


FIG. 6: The off-resonant Raman scattering processes lead to the on-site term and the off-site term in Eqn.29.

The interaction between the two laser beams in Fig.1 with the two level bosonic atoms is:

$$H_{int} = \int d^2\vec{r} \Psi^\dagger(\vec{r}) [\frac{\vec{p}^2}{2m_a} + V_{OL}(\vec{r}) + \frac{\hbar\omega_a}{2} \sigma_z + \frac{\Omega}{2} \sum_l (e^{-i\omega_l t} \sigma^+ u_l(\vec{r}) + h.c.)] \Psi(\vec{r}) \quad (28)$$

where $\Psi(\vec{r}) = (\psi_e, \psi_g)$ is the two component boson annihilation operator, the incident and scattered lights in Fig.1a and the two incident lights in Fig.1b have frequencies ω_l and mode functions $u_l(\vec{r}) = e^{i\vec{k}_l \cdot \vec{r} + i\phi_l}$. The Rabi frequencies Ω are much weaker than the laser beams (not shown in Fig.1) which form the optical lattices. In the following, we develop the formalism by using the light scattering geometry in Fig.1a which also applies to the atom scattering geometry in Fig.1b after some slight modifications. When it is far off the resonance, the laser light-atom detunings $\Delta_l = \omega_l - \omega_a$ where ω_a is the two level energy difference are much larger than the Rabi frequency Ω and the energy transfer $\omega = \omega_1 - \omega_2$ (See Fig.6), so $\Delta_1 \sim \Delta_2 = \Delta$. After adiabatically eliminating the upper level e of the two level atoms, expanding the ground state atom field operator $\psi_g(\vec{r}) = \sum_i b_i w(\vec{r} - \vec{r}_i)$ in Eqn.28 where $w(\vec{r} - \vec{r}_i)$ is the localized Wannier functions of the lowest Bloch band corresponding to $V_{OL}(\vec{r})$ and b_i is the annihilation operator of an atom at the site i in the Eqn.1, then we get the effective interaction between the off-resonant laser beams and the ground level g :

$$H_{int} = \hbar \frac{\Omega^2}{\Delta} e^{-i\omega t} [\sum_i^N J_{i,i} n_i + \sum_{<ij>}^N J_{i,j} b_i^\dagger b_j] \quad (29)$$

where the interacting matrix element is $J_{i,j} = \int d\vec{r} w(\vec{r} - \vec{r}_i) u_1^*(\vec{r}) u_2(\vec{r}) w(\vec{r} - \vec{r}_j) = J_{j,i}$. The first term in Eqn.29 is the on-site term $\hat{D} = \sum_i^N J_{i,i} n_i$ (See Fig.6a). The second term is the off-site term (See Fig.6b). Because the Wannier wavefunction $w(\vec{r})$ can be taken as real in the lowest Bloch band³², the off-site term can be written as $\hat{K} = \sum_{<ij>}^N J_{i,j} b_i^\dagger b_j = \sum_{<ij>}^N J_{i,j} (b_i^\dagger b_j + h.c.)$ which is nothing but the off-site coupling to the nearest neighbor kinetic energy of the bosons $K_{ij} = b_i^\dagger b_j + h.c..$

It is easy to show that:

$$\hat{D}(\vec{q}) = f_0(\vec{q}) \sum_{i=1}^N e^{-i\vec{q} \cdot \vec{r}_i} n_i = N f_0(\vec{q}) n(\vec{q}) \quad (30)$$

where $\vec{q} = \vec{k}_1 - \vec{k}_0$, $f_0(\vec{q}) = \int d\vec{r} e^{-i\vec{q} \cdot \vec{r}} w^2(\vec{r})$ and $n(\vec{q}) = \frac{1}{N} \sum_{i=1}^N e^{-i\vec{q} \cdot \vec{r}_i} n_i = \sum_{\vec{k}} b_{\vec{k}}^\dagger b_{\vec{k}+\vec{q}}$ is the Fourier transform of the density operator at the momentum \vec{q} . The wavevector is confined to $L^{-1} < q < a^{-1}$ where the trap size $L \sim 100\mu m$ and the lattice constant $a \sim 0.5\mu m$ in Fig.1. In fact, more information is encoded in the off-site kinetic coupling in Eqn.29. In a square lattice, the bonds are either oriented along the \hat{x} axis $\vec{r}_j - \vec{r}_i = \hat{x}$ or along the \hat{y} axis $\vec{r}_j - \vec{r}_i = \hat{y}$, we have:

$$\hat{K}_{\square} = N [f_x(\vec{q}) K_x(\vec{q}) + f_y(\vec{q}) K_y(\vec{q})] \quad (31)$$

where $K_{\alpha}(\vec{q}) = \frac{1}{N} \sum_{i=1}^N e^{-i\vec{q} \cdot \vec{r}_i} K_{i,i+\alpha} = e^{iq_{\alpha}/2} \sum_{\vec{k}} \cos k_{\alpha} b_{\vec{k}}^\dagger b_{\vec{k}+\vec{q}}$ are the Fourier transform of the kinetic energy operator $K_{ij} = b_i^\dagger b_j + h.c.$ along $\alpha = x, y$ bonds at the momentum \vec{q} and the "form" factors $f_{\alpha}(\vec{q}) = f(\vec{q}, \vec{r}_i - \vec{r}_j = \alpha) = \int d\vec{r} e^{-i\vec{q} \cdot \vec{r}} w(\vec{r}) w(\vec{r} + \vec{r}_i - \vec{r}_j)$. Following the harmonic approximation used in³, we can estimate that:

$$f_0(\pi, 0) \sim e^{-\frac{1}{4}(V_0/E_r)^{-1/2}} \\ f_x(\pi, 0) \sim ie^{-\frac{1}{4}(V_0/E_r)^{-1/2} - \frac{\pi^2}{4}(V_0/E_r)^{1/2}} \quad (32)$$

so $|f_x(\pi, 0)/f_0(\pi, 0)| \sim e^{-\frac{\pi^2}{4}\sqrt{V_0/E_r}}$ where V_0 and $E_r = \hbar^2 k^2 / 2m$ are the strength of the optical lattice potential and the recoil energy respectively³. The $f_0(\pi, 0)$ is close to 1 when $V_0/E_r > 4$. It is instructive to relate this ratio to that of the hopping t over the onsite interaction U in the Eqn.1: $|f_x(\pi, 0)/f_0(\pi, 0)| \sim \frac{t}{U} \frac{a_s}{a}$ where a_s is the zero field scattering length and $a = \lambda/2 = \pi/k$ is the lattice constant, using the typical values $t/U \sim 10^{-1}$, $a_s/a \sim 10^{-2}$, one can estimate $|f_x/f_0| \sim 10^{-3}$. Note that the harmonic approximation works well only in a very deep optical lattice $V_0 \gg E_r$, so the above value underestimates the ratio, so we expect $|f_x/f_0| \geq 10^{-3}$.

The differential scattering cross section of the light from the cold atom systems in the Fig.1 can be calculated by using the standard linear response theory:

$$\frac{d\sigma}{d\Omega dE} \sim (\frac{\Omega^2}{\Delta})^2 N^2 [|f_0(\vec{q})|^2 S_n(\vec{q}, \omega) + \sum_{\alpha=\hat{x}, \hat{y}} |f_{\alpha}(\vec{q})|^2 S_{K_{\alpha}}(\vec{q}, \omega)] \quad (33)$$

where $\vec{q} = \vec{k}_1 - \vec{k}_0$, $\omega = \omega_1 - \omega_2$, the $S_n(\vec{q}, \omega) = \langle n(-\vec{q}, -\omega) n(\vec{q}, \omega) \rangle$ is the dynamic density-density response function whose Lehmann representation was listed in⁵. The $S_{K_{\alpha}}(\vec{q}, \omega) = \langle K_{\alpha}(-\vec{q}, -\omega) K_{\alpha}(\vec{q}, \omega) \rangle$ is the bond-bond response function whose Lehmann representation can be got from that of the $S_n(\vec{q}, \omega)$ simply by replacing the density operator $n(\vec{q})$ by the bond operator $K_{\alpha}(\vec{q})$.

The elastic scattering cross section $\frac{d\sigma}{d\Omega}|_{el}$ is proportional to:

$$\begin{aligned} \frac{d\sigma}{d\Omega}|_{el} &= \left(\frac{\Omega^2}{\Delta}\right)^2 N^2 [|f_0(\vec{q})|^2 S_n(\vec{q}, \omega = 0) \\ &+ \sum_{\alpha=\hat{x},\hat{y}} |f_\alpha(\vec{q})|^2 S_{K_\alpha}(\vec{q}, \omega = 0)] \end{aligned} \quad (34)$$

The integrated differential scattering cross section over the final energy $\frac{d\sigma}{d\Omega} = \int d\omega \frac{d\sigma}{d\Omega d\omega}$ is proportional to the equal-time response function is

$$\begin{aligned} \frac{d\sigma}{d\Omega} &= \left(\frac{\Omega^2}{\Delta}\right)^2 N^2 [|f_0(\vec{q})|^2 S_n(\vec{q}) \\ &+ \sum_{\alpha=\hat{x},\hat{y}} |f_\alpha(\vec{q})|^2 S_{K_\alpha}(\vec{q})] \end{aligned} \quad (35)$$

In the following, we will discuss the physical implications of Eqn.33 on the CDW, VBS and corresponding supersolids summarized in the Sec.II.

V. SUPERFLUID, MOTT INSULATOR AND SUPERFLUID TO MOTT TRANSITION AT INTEGER FILLINGS

Quantum phase transitions are characterized by three critical exponents z, ν, η called "two scale factor" universality. It is well known that the SF to Mott transition is described by the relativistic effective action^{2,29}:

$$\mathcal{S} = \int d^2 r d\tau [|(\partial_\tau \phi)^2 + |\nabla \phi|^2 + r|\phi|^2 + u|\phi|^4 + \dots] \quad (36)$$

where in the Mott state $r > 0, \langle \phi \rangle = 0$, while in the SF phase $r < 0, \langle \phi \rangle \neq 0$. The SF to Mott transition described by Eqn.36 is in the $3d$ XY universality class with the critical exponents $z = 1, \nu = 0.67, \eta = 0.04$ (Note that for $d = 1$, it is in $2d$ XY universality class, namely, KT transition). In the following, we will discuss the elastics and the in-elastic scattering at the SF and Mott, then the quantum phase transition between the two phases respectively.

(a) *Elastics scattering at the reciprocal lattice vector \vec{K} to detect SF and Mott states*

We first look at the superfluid to Mott transition at integer filling factor n . When \vec{q} is equal to the shortest reciprocal lattice vector $\vec{K} = (2\pi, 0)$, in the Mott state, $\frac{d\sigma^M}{d\Omega} \sim |f_0^M(2\pi, 0)|^2 N^2 n^2$, in the superfluid state, $\frac{d\sigma^M}{d\Omega} \sim |f_0^{SF}(2\pi, 0)|^2 N^2 n^2 + 2|f_x^{SF}(2\pi, 0)|^2 N^2 B^2$ where B is the average kinetic energy on a bond in the superfluid side. Because $|f_0^{SF}(2\pi, 0)|^2 \sim |f_0^M(2\pi, 0)|^2 \sim 1$ and B is appreciable only in the superfluid side, we expect an increase of the scattering cross section:

$$\frac{d\sigma^{SF}}{d\Omega} - \frac{d\sigma^M}{d\Omega} \sim 2|f_x^{SF}(2\pi, 0)|^2 N^2 B^2 \quad (37)$$

across the Mott to the SF transition due to the prefactor N^2 . This increase may be used as an effective measure

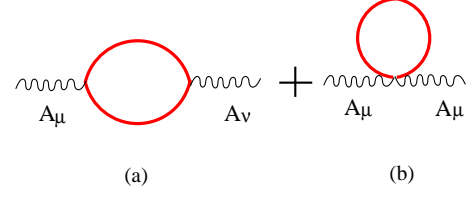


FIG. 7: The current-current correlator. Its $\mu = \nu = 0$ component leads to the boson density-density correlation function Eqn.40. Although the $D = 3+1$ case was well documented⁴⁹. The $D = 2+1$ case seems not be calculated yet and was done in the Sec.V-b.

of the boson kinetic energy inside the SF. This prediction could be tested immediately. Surprisingly, there is no such optical Bragg scattering experiment in the superfluid yet.

(b) *In-elastics scattering slightly away from a reciprocal lattice vector \vec{K} to detect the excitation spectrum in SF and Mott states*

Now we study the in-elastic scattering away from zero (or any other reciprocal lattice vector \vec{K}). The excitation spectrum inside a SF was already given in Eqn.12 and Eqn.13. Here, from the effective theory of both boson and dual vortex pictures, we will calculate the density-density correlation function not only in the SF side, but also in the Mott side and the quantum critical point. Although the order parameter correlation functions were well studied from both the direct and dual pictures, but it seems the density-density correlation functions have not been discussed so far.

(1) *Density-density correlation functions from a direct boson picture*

Observing that the density $n = \phi^\dagger \partial_\tau \phi - (\partial_\tau \phi^\dagger) \phi$ is a conserved quantity. In order to calculate the density-density correlation function, we add a source term to Eqn.36

$$\mathcal{S}[A_\mu, \phi] = \int d^2 r d\tau [|(\partial_\mu - iA_\mu)\phi|^2 + m^2|\phi|^2 + u|\phi|^4 + \dots] \quad (38)$$

In the Mott side, $m^2 > 0$, Then integrating out the massive ϕ field according to the Feynmann diagram Fig.7 paying special attentions to the diamagnetic term in Fig.7b, one gets

$$\begin{aligned} \mathcal{S}[A_\mu] &= \frac{1}{2} A_\mu(-k) \Pi_{\mu\nu}(k) A_\nu(k) + \dots \\ \Pi_{\mu\nu}(k) &= \frac{m}{2\pi} \left[\frac{k_\mu k_\nu}{k^2} - \delta_{\mu\nu} \right] (I(z) - 1), \quad z = \frac{k^2}{m^2} \end{aligned} \quad (39)$$

where $I(z) = \int_0^1 dx [1 + x(1 - x)z]^{1/2} = \frac{1}{2} + \frac{(4+z)}{4\sqrt{z}} \arctan \frac{\sqrt{z}}{2} = 1 + \frac{z}{12} - \frac{z^2}{240} + \dots$ as $z \rightarrow 0$.

Using $A_\mu = (A_0, A_\alpha)$ and $k = (\omega, \vec{q})$ and putting $\mu = \nu = 0$, we can get the boson density-density correlation function:

$$S_n(\vec{q}, \omega) = \Pi_{00}(\vec{q}, \omega) = \frac{5m}{6\pi} \frac{q^2}{\omega^2 + q^2 + 20m^2} \quad (40)$$

where one can identify the Mott gap $\Delta_{Mott}^2 = 20m^2$. The compressibility $\kappa = S(\vec{q} \rightarrow 0, \omega = 0) \sim q^2 \rightarrow 0$, namely, in-compressible inside the Mott state as expected.

One can evaluate immediately the structure factor

$$S_n(\vec{q}) = \frac{5m}{12\pi} \frac{q^2}{\sqrt{q^2 + 20m^2}} \quad (41)$$

At the quantum critical point between the SF and the Mott phase, $m \rightarrow 0$, $z \rightarrow \infty$, then $I(z) \rightarrow \sqrt{z} \int_0^1 \sqrt{x(1-x)} = \frac{\pi}{8} \sqrt{z}$, we get

$$S_n^{QC}(\vec{q}, \omega) = \frac{1}{16} \frac{q^2}{\sqrt{\omega^2 + q^2}} \quad (42)$$

which shows that $\kappa = S(\vec{q} \rightarrow 0, \omega = 0) \sim q \rightarrow 0$, namely, still in-compressible at the QC point.

One can evaluate immediately the dynamic structure factor

$$S_n^{QC}(\vec{q}) \sim q^2 \log \Lambda/q \quad (43)$$

where the Λ is the ultra-violet frequency cutoff.

In summary, from Eqn.12, 40, 42, in the Mott state, when $q \ll m$, one can see $S^{Mott}(\vec{q}) \sim q^2$ which is in sharp contrast to that inside a superfluid $S^{SF}(\vec{q}) \sim q$. While at the QC, $S^{QC}(\vec{q}) \sim q^2 \log \Lambda/q$.

Inside the superfluid $m^2 < 0$, then it is convenient to write $V(\phi) = \frac{1}{4}\lambda(|\phi|^2 - a^2)^2$. We write the order parameter in the polar coordinate $\phi = \sqrt{a^2 + \delta\rho}e^{i\phi}$, then Eqn.36 becomes:

$$\begin{aligned} \mathcal{L} = & (a^2 + \delta\rho)(\partial_\mu\theta)^2 + \dots \\ & + \frac{1}{4}(a^2 + \delta\rho)^{-1}(\partial_\mu\delta\rho)^2 + \frac{1}{4}\lambda(\delta\rho)^2 \end{aligned} \quad (44)$$

where one can see that there is a gapless (Goldstone) θ mode and the massive magnitude $\delta\rho$ fluctuation mode. Unfortunately, it is not straightforward to extract the density-density correlation function inside a SF from Eqn.44. However, as shown below, it can be easily derived from the dual vortex picture.

The scattering cross section at the classical diffraction minimum $\vec{q} = (\pi, \pi)$ will be computed in the appendix A.

(2) *The density-density correlation functions from a dual vortex picture*

Alternatively, one can calculate the density-density correlation from the dual vortex action^{29,47}. It is well known that the boson action Eqn.36 is dual to the vortex action:

$$\begin{aligned} \mathcal{S}_d[a_\mu, \psi] = & \int d^3x [(\partial_\mu - ia_\mu)\psi]^2 + r_d|\psi|^2 + u_d|\psi|^4 + \dots \\ & + \frac{1}{4e^2}f_{\mu\nu}^2 \end{aligned} \quad (45)$$

where in the Mott state $r_d < 0$, $\langle\psi\rangle \neq 0$, while in the SF phase $r_d > 0$, $\langle\psi\rangle = 0$ with also the 3d XY critical exponents $z = 1$, $\nu = 0.67$, $\eta = 0.04$.

In the Mott state, the vortex condensation $\langle\psi\rangle \neq 0$ leads to a mass term for the gauge field $\frac{1}{2}|\langle\psi\rangle|^2(a_\mu^t)^2$ where a_μ^t is the transverse component of the gauge field. In the Landau gauge $\partial_\mu a_\mu = 0$, the effective action for the gauge field is:

$$\begin{aligned} \mathcal{S}_d[a_\mu] = & \frac{1}{2}a_\mu(-k)[\frac{k^2}{e^2}(\delta_{\mu\nu} - \frac{k_\mu k_\nu}{k^2}) + \frac{1}{\alpha}k_\mu k_\nu \\ & + |\langle\psi\rangle|^2(\delta_{\mu\nu} - \frac{k_\mu k_\nu}{k^2})]a_\nu(k) \end{aligned} \quad (46)$$

where $\alpha \rightarrow 0$ indicates the Landau gauge.

Using $a_\mu = (a_0, \vec{a})$ and $k = (\omega, \vec{q})$, we can find the density-density correlation inside the Mott phase:

$$S_n^{Mott}(\vec{q}, \omega) = \langle(\nabla \times \vec{a})(\nabla \times \vec{a})\rangle = \frac{e^2 q^2}{\omega^2 + q^2 + m_d^2} \quad (47)$$

where $m_d^2 = e^2|\langle\psi\rangle|^2$. We can identify the quasi-particle spectral weight $\mathcal{A} = e^2$. It is identical to Eqn.40 after we identify $m_d^2 = 20m^2$.

Inside the superfluid state $r_d > 0$, the mass term for the gauge field is absent, integrating out the massive vortex fluctuation leads to the density-density correlation inside the superfluid phase:

$$S_n^{SF}(\vec{q}, \omega) = \langle(\nabla \times \vec{a})(\nabla \times \vec{a})\rangle = \frac{e^2 q^2}{\omega^2 + q^2} \quad (48)$$

which is identical to Eqn.12 after putting back the corresponding the superfluid density ρ_s and the phonon velocity v^2 .

At the quantum critical point between the SF and the Mott phase, integrating out the massless vortex fluctuation leads to the density-density correlation at the QC:

$$S_n^{QC}(\vec{q}, \omega) \sim \langle(\nabla \times \vec{a})(\nabla \times \vec{a})\rangle = \frac{q^2}{\sqrt{\omega^2 + q^2}} \quad (49)$$

which is identical to Eqn.42 from the direct boson picture. Eqn.43 follows.

(c) *The scaling functions across the SF to Mott transition*

So far, we discussed the properties of different quantum phases where mean field theory works well. It is important to study quantum fluctuations near the quantum critical point between different quantum phases. Ref.² focused on the scaling form of the single particle Green function $\langle\phi^\dagger(\vec{x}, \tau)\phi(0, 0)\rangle$. Here, motivated by the light scattering experiments, we are studying the scaling form of the density-density correlation function $\langle\delta n(\vec{x}, \tau)\delta n(0, 0)\rangle$ where $\delta n = \phi^\dagger\partial_\tau\phi - (\partial_\tau\phi^\dagger)\phi$. Following the scaling theory developed in⁴⁵ and observing δn is a conserved quantity, we can write down the scaling functions near the SF to Mott transition in Fig.8:

$$S_n(\vec{q}, \omega, k_B T) = |C|^2 \frac{k_B T}{v^2} \Phi_{SF}(\frac{\hbar v q}{k_B T}, \frac{\hbar \omega}{k_B T}, \frac{k_B T}{2\pi\rho_s}) \quad (50)$$

In the Mott state $2\pi\rho_s$ should be replaced by the Mott gap Δ . At the QC, $\Phi_{SF}(\frac{\hbar v q}{k_B T}, \frac{\hbar \omega}{k_B T}, \infty) =$

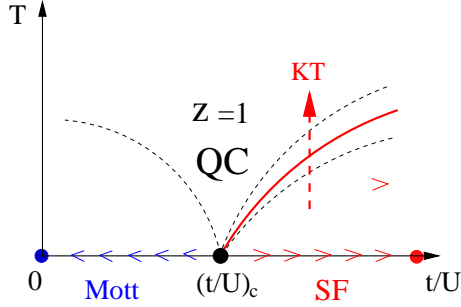


FIG. 8: Finite temperature phase diagram of the SF to Mott transition. There are 3 fixed points: the Mott fixed point at $t/U = 0$, the SF fixed point at $t/U = \infty$ and the quantum critical point at $(t/U)_c$. The QC is the quantum Critical regime. The KT stands for the Kosterlize-Thouless transition. See Fig.15 for the zero temperature phase diagram and the phases inside a trap.

$\Phi_{Mott}(\frac{\hbar v q}{k_B T}, \frac{\hbar \omega}{k_B T}, \infty)$. Note that due to $z = 1$, the spin wave velocity v remains not critical across the SF to Mott transition in Fig.8, while $\rho_s \sim (t - t_c)^\nu$, $\Delta \sim (t_c - t)^\nu$, $\nu \sim 0.67$.

Note that Eqn.12 in the SF and Eqn.40 in the Mott side only work deep inside the two phases controlled by the SF fixed point and the Mott fixed point in Fig.8 respectively, but will break down near to the QCP. The equal time correlation function follow from $\int \frac{d\omega}{2\pi}$ over Eqn.50.

At $T = 0$, Eqn.50 simplifies to

$$S_n(\vec{q}, \omega, T = 0) = |C|^2 \frac{2\pi \rho_s}{v^2} \Phi_{SF}(\frac{\hbar v q}{2\pi \rho_s}, \frac{\hbar \omega}{2\pi \rho_s}) \quad (51)$$

In the Mott state $2\pi \rho_s$ should be replaced by the Mott gap Δ . From Eqn.12, we can determine that $\Phi_{SF}(x, y) = \frac{x^2}{x^2 + y^2}$. From Eqn.40, we can determine that $\Phi_{Mott}(x, y) = \frac{x^2}{x^2 + y^2 + 1}$.

At the QC $\rho_s = \Delta = 0$, Eqn.51 simplifies further to

$$S_n^{QC}(\vec{q}, \omega, T = 0) = |C|^2 \frac{\hbar v q}{v^2} \Phi_{QC}(\frac{\hbar \omega}{\hbar v q}) \quad (52)$$

From Eqn.42, we can determine that $\Phi_{QC}(x) = \frac{1}{\sqrt{x^2 + 1}}$.

VI. CDW AND CDW SUPERSOLID AT AND NEAR HALF FILLINGS

At the 1/2 filling along the horizontal axis in Fig.3a, inside the SF state near the CDW, there is a peak of $S_n(\vec{q})$ near $\vec{Q}_n = (\pi, \pi)$, so the SF to the CDW transition is a first order one driven by the instability of the peak. Due to the lack of VBS order on both sides, the second term in Eqn.33 can be neglected, so that

$$\frac{d\sigma}{d\Omega dE}|_{CDW} \sim (\frac{\Omega^2}{\Delta})^2 N^2 |f_0(\vec{q})|^2 S_N(\vec{q}, \omega) \quad (53)$$

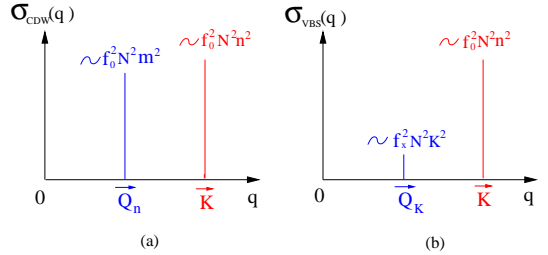


FIG. 9: The characteristics of optical scattering cross section in a square lattice.(a) CDW, the ratio of the peak at \vec{Q}_n over that at \vec{K} is $\sim m^2/n^2 \sim 1$. (b) VBS state, the ratio of the peak at \vec{Q}_K over that at \vec{K} is $\sim |f_x/f_0|^2 K^2/n^2 \sim 10^{-5}$. It should be visible in the current optical Bragg scattering experiments.

(a) Elastic scattering at the CDW and CDW-SS ordering vector \vec{Q}_n .

When one gets into the CDW state at \vec{Q}_n in Fig.3b in²⁹, then the $S_n(\vec{q})$ should show a peak at $\vec{q} = \vec{Q}_n$ whose amplitude scales as the square of the number of atoms inside the trap $S_{CDW}(\vec{Q}_n) \sim |f_0(\pi, \pi)|^2 N^2 m^2$ where $m = n_A - n_B$ is the CDW order parameter²⁹. When $\vec{q} = \vec{K}$, then $S_{CDW}(\vec{K}) \sim |f_0(2\pi, 0)|^2 N^2 n^2$ where $f_0(2\pi, 0) \sim f_0^2(\pi, \pi)$ (Fig.9a). So the ratio of the two peaks in Fig.9a is $S_{CDW}(\vec{Q}_n)/S_{CDW}(\vec{K}) \sim m^2/n^2$ if one neglects the small difference of the two form factors. Slightly away from 1/2 filling, the CDW in Fig.3a may turn into the CDW supersolid (CDW-SS) phase through a second order phase transition described by Eqn.54. Then we have $\langle n(\vec{q}) \rangle = m\delta_{\vec{q}, \vec{Q}_n} + n\delta_{\vec{q}, 0}$ where $n = n_A + n_B = 1/2 + \delta n$. The superfluid density $\rho_s \sim \delta n = n - 1/2$. The scattering cross section inside the CDW-SS at \vec{Q}_n : $S_{CDW-SS}(\vec{Q}_n) \sim |f_0(\pi, \pi)|^2 N^2 m^2$ stays more or less the same as that inside the CDW, but at $\vec{K} = (2\pi, 0)$: $S_{CDW-SS}(\vec{K}) \sim |f_0(2\pi, 0)|^2 N^2 n^2 + 2|f_x(2\pi, 0)|^2 N^2 (\delta n)^2 B^2$ will increase where $n = 1/2 + \delta n$. The B is the average bond strength due to very small superfluid component $\rho_s \sim \delta n = n - 1/2$ flowing through the whole lattice. So we expect the right peak in Fig.9a will increase due to the increase of the total density and the superfluid component inside the CDW-SS phase. Of course, the small superfluid component at $\vec{k} = 0$ can also be detected by the TOF with the peak strength near $\vec{k} = 0$ proportional to $\rho_s \sim \delta n$.

(b) In-elastics scattering to detect the excitation spectrum in CDW and CDW-SS

So far, we only discussed the ground state properties of various quantum states. The elementary excitation spectrum above these ground states can be determined from the peak positions of the corresponding dynamic density-density or bond-bond response functions. Eqn.33 shows that the response function of the cold atom system is the sum of the two response functions with the corresponding spectral weight $\sim |f_0|^2$ and $\sim |f_\alpha|^2$. The $\langle \delta n \delta n \rangle$ correla-

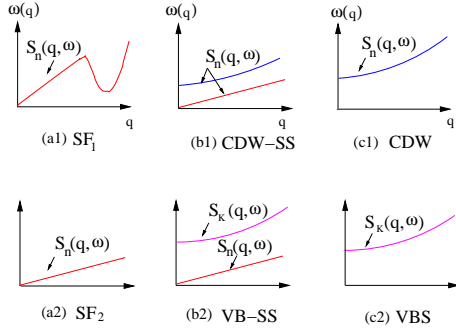


FIG. 10: The excitations spectrum in the CDW, VBS, SF, CDW-SS and VB-SS states which are the peak positions of the corresponding dynamic response functions shown with arrows. In the (b1) and (c1) cases, the starting wavevector is \vec{Q}_n in the upper CDW branch. In the (b2) and (c2) cases, the starting wavevector is \vec{Q}_K in the upper VBS branch. The corresponding spectral weights are worked out in the text.

tion function inside a SF was studied in several different physical systems in^{43,44} and was listed in Eqn.12 and 13. In the SF near to the CDW, there is a roton minimum near $\vec{q} = \vec{Q}_n$, the $S_n(\vec{q})$ shows a peak near \vec{Q}_n in Fig.10a1. The superfluid mode in the Fig.10a1 has a spectral weight $\sim N|f_0|^2 \times \rho_s$ where $\rho_s \sim n$. Inside the CDW-SS, the roton minimum disappears and is replaced by the upper branch with a CDW gap $\Delta_{CDW} \sim U$ and a spectral weight $\sim N|f_0|^2 \times 1/2$ in the Fig.10b1, the lower superfluid branch in the Fig.10b1 has a spectral weight $\sim N|f_0|^2 \times \rho_s$ where $\rho_s \sim \delta n = n - 1/2$ is the superfluid density inside the CDW-SS. Inside the CDW, the superfluid lower branch disappears, the upper CDW branch in Fig.10c1 has the spectral weight $\sim N|f_0|^2 \times 1/2$.

(c) *Scaling function across the CDW to CDW-SS transition.*

Slightly away from 1/2 filling, the transition from the CDW to the CDW-SS along the vertical axis in Fig.3b is described by the *non-relativistic effective action*²⁹:

$$\begin{aligned} S_{non} = & \int d^2r d\tau [\phi^\dagger \partial_\tau \phi + |\partial_\tau \phi|^2 + \frac{\hbar^2}{2m_a} |\nabla \phi|^2 \\ & - \mu |\phi|^2 + u |\phi|^4 + \dots] \end{aligned} \quad (54)$$

with the critical exponents $z = 2$, $\nu = 1/2$, $\eta = 0$ with logarithmic corrections²⁹. It is the chemical potential μ tuning the zero density transition from the CDW at $\mu < 0$ with $\langle \phi \rangle = 0$ to the CDW-SS with $\mu > 0$ with $\langle \phi \rangle \neq 0$. Ref.⁴⁶ focused on the scaling form of the single particle Green function $\langle \phi^\dagger(\vec{x}, \tau) \phi(0, 0) \rangle$. Here, motivated by the light scattering experiments, we are studying the scaling form of the density-density correlation function $\langle \delta n(\vec{x}, \tau) \delta n(0, 0) \rangle$ where $\delta n = \phi^\dagger \phi$ is the density above the CDW background.

Well inside the CDW-SS phase, one can set $\langle \phi \rangle = |\langle \phi \rangle| e^{i\theta}$, then the linear derivative term in Eqn.54 becomes irrelevant, the density-density correlation function of the SF component reduces to Eqn.12 with $\rho_s \sim$

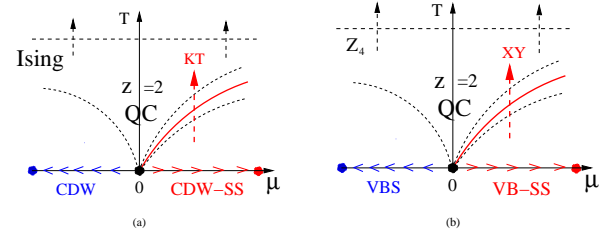


FIG. 11: (a) The CDW to CDW-SS driven by the chemical potential μ . The dashed line is a finite temperature Ising melting transition. (b) The VBS to VB-SS driven by the chemical potential μ . The dashed line is a finite temperature Z_4 Clock melting transition. See also Fig.3 for the zero temperature phase diagram and Fig.16 for the phases inside a trap.

$\frac{\hbar^2 |\langle \phi \rangle|^2}{2m_a}$. It leads to the lower branch in Fig.10b1. Near to the QCP, we have $\langle n(\vec{q}) \rangle = m \delta_{\vec{q}, \vec{Q}_n} + n \delta_{\vec{q}, 0}$ where $n = n_A + n_B = 1/2 + \delta n$. Because $\delta n = \phi^\dagger \phi$ is a conserved quantity, so it has no anomalous dimension. From the scaling analysis in⁴⁶, one can show that at $T = 0$

$$\delta n = \frac{m_a \mu a^2}{4\pi \hbar^2} \ln \left[\frac{\hbar^2}{2m_a \mu a^2} \right] \quad (55)$$

where a is the lattice constant and m_a is the effective atom mass in Eqn.54 and 28. In the scaling limit $q \ll 1/a$, $\hbar \omega \ll \frac{\hbar^2}{2m_a q^2}$, the density-density correlation function should take the following scaling form:

$$S_n(\vec{q}, \omega) = \frac{2m_a a^4}{\hbar^2} \Phi_n \left(\frac{\hbar \omega}{k_B T}, \frac{\hbar q}{\sqrt{2m_a k_B T}}, \frac{\mu}{k_B T} \right) \quad (56)$$

upto a logarithmic factor where Φ_n is a universal function independent of the atom-atom interactions in Eqn.1. Inside the CDW-SS phase in Fig.3b, there should also be a $S_n(\vec{q})$ peak $\sim |f_0|^2 N^2 m^2$ at $\vec{q} = \vec{Q}_n$ signaling its CDW order.

VII. VBS AND VBS SUPERSOLID AT AND NEAR HALF FILLINGS

At the 1/2 filling along the horizontal axis in Fig.3b, inside the SF state near the VBS, there is a peak of $S_K(\vec{q})$ near $\vec{Q}_K = (\pi, 0)$, so the SF to the VBS transition is a very weak first order one.

(a) *Elastic scattering at the VBS and VB-SS ground state at its ordering wavevector \vec{Q}_K .*

When $\vec{q} = \vec{K}$, due to the *uniform* distribution of the density in the VBS, the second term in Eqn.33 can be neglected, so there is a diffraction peak (Fig.9b) whose amplitude scales as the *square* of the number of atoms inside the trap $S_{VBS}(\vec{K}) \sim |f_0(2\pi, 0)|^2 N^2 n^2$ where $f_0(2\pi, 0) \sim f_0^4(\pi, 0)$ and $n = 1/2$ is the uniform density in the VBS state.

However, when one tunes \vec{q} near \vec{Q}_K , the first term in

Eqn.33 can be neglected, then

$$\frac{d\sigma}{d\Omega dE}|_{VBS} \sim \left(\frac{\Omega^2}{\Delta}\right)^2 N^2 \sum_{\alpha=\hat{x},\hat{y}} |f_\alpha(\vec{q})|^2 S_{K_\alpha}(\vec{q},\omega) \quad (57)$$

It should show a peak at $\vec{q} = \vec{Q}_K$ signifying the VBS ordering at \vec{Q}_K whose amplitude scales also as the square of the number of atoms inside the trap $S_{VBS}(\vec{Q}_K) \sim |f_x(\pi,0)|^2 N^2 K^2$ where $K = K_x - K_y$ is the VBS order parameter²⁹. So the ratio of the VBS peak at $\vec{q} = \vec{Q}_K$ over the uniform density peak at $\vec{q} = \vec{K}$ is $S_{VBS}(\vec{Q}_K)/S_{VBS}(\vec{K}) \sim |f_x(\pi,0)/f_0(2\pi,0)|^2 \geq 10^{-5}$. However, the smallness of $|f_x|^2$ is compensated by the large number of atoms $N \sim 10^6$, $|f_x|^2 N^2 = (|f_x|^2 N) \times N \sim N \sim 10^6$. Therefore, the Bragg scattering cross section from the VBS order is $\geq 10^{-5}$ smaller than that at $\vec{q} = \vec{K}$ at the same incident energy I_{in} (Fig.9b), but still $\sim 10^6$ above the background, so very much visible in the current optical Bragg scattering experiments. Slightly away from 1/2 filling, the VBS may turn into VB Supersolid (VB-SS) through a second order transition²⁹. We have $\langle K_x(\vec{q}) \rangle = B\delta_{\vec{q},0} + K\delta_{\vec{q},\vec{Q}_K}$ and $\langle n(\vec{q}) \rangle = (\delta n + 1/2)\delta_{\vec{q},0}$. The superfluid density $\rho_s \sim \delta n = n - 1/2$. The scattering cross section inside VB-SS: $S_{VB-SS}(\vec{Q}_K) \sim |f_x(\pi,0)|^2 N^2 K^2$ stays more or less the same as that inside the VBS, but $S_{VB-SS}(\vec{K}) \sim |f_0(2\pi,0)|^2 N^2 n^2 + |f_x(2\pi,0)|^2 N^2 (\delta n)^2 B_x^2 + |f_y(2\pi,0)|^2 N^2 (\delta n)^2 B_y^2$ where $n = 1/2 + \delta n$ and the B_x, B_y are the average bond strengths along x and y due to very small superfluid component $\rho_s \sim \delta n = n - 1/2$ flowing through the whole lattice. So we expect the right peak in Fig.9b will increase due to the increase of the total density and the superfluid component inside the VB-SS phase. Of course, the superfluid component at $\vec{k} = 0$ can also be detected by the TOF with the peak strength near $\vec{k} = 0$ proportional to $\rho_s \sim \delta n$. Very similarly, one can discuss the VBS order at $\vec{q} = \vec{Q}_K = (0,\pi)$. For the plaquette VBS order in Fig.2 which has both $(\pi,0)$ and $(0,\pi)$ order, then one should be able to see the $S_K(\vec{q})$ peaks at both $(\pi,0)$ and $(0,\pi)$. So the dimer VBS and the plaquette VBS can also be distinguished by the optical Bragg scattering.

(b) *In-elastics scattering to detect the excitation spectrum in VBS and VB-SS*

In the SF near to the VB, there is no peak in $S_n(\vec{q})$. The superfluid mode in the Fig.10a2 has a spectral weight $\sim N|f_0|^2 \times \rho_s$ where $\rho_s \sim n$. However, $S_{VBS}(\vec{q})$ shows a peak near \vec{Q}_K which is suppressed by a factor $|f_x|^2$ as compared to Fig.10a1. Inside the VB-SS, the SF order of the VB-SS is the same as the SF inside the CDW-SS, so its $\langle \delta n \delta n \rangle$ correlation function is also given by Eqn.12. So there is a upper branch with a VBS gap $\Delta_{VBS} \sim t^2/U$ and a spectral weight $\sim N|f_x|^2 \times 1/2$ in the Fig.10b2, also a lower superfluid branch in the Fig.10b2 with the spectral weight $\sim N|f_0|^2 \times \rho_s$ where $\rho_s \sim \delta n = n - 1/2$ is the superfluid density inside the VB-SS. Inside the VBS, the superfluid lower branch disappears, the upper VBS branch in Fig.10c2 has the spectral weight $\sim N|f_x|^2 \times$

1/2.

(c) *The transition from the VBS to the VB-SS*

Slightly away from 1/2 filling, the transition from the VBS to the VB-SS along the vertical axis in Fig.3b near $\vec{q} = (0,0)$ is also described by Eqn.54, so it is also in the same universality class of SF to Mott transition with the critical exponents $z = 2, \nu = 1/2, \eta = 0$ upto a logarithmic correction²⁹. Eqn.55 and Eqn.56 also hold with $\delta n = \phi^\dagger \phi$ as the boson density above the VBS background.

VIII. EXTENSION TO FRUSTRATED LATTICES

The procedures discussed in bipartite lattices in the previous sections can be generalized to frustrated lattices such as triangular and kagome lattices. There are several new features due to the frustrations (1) The ordering wavevector $\vec{Q}_n \neq -\vec{Q}_n$, while for a bi-partite lattice $\vec{Q}_n = -\vec{Q}_n$ upto a reciprocal lattice. (2) The corresponding fluctuation near the ordering wavevector \vec{Q}_n will be a complex order parameter, in contrast to that on a bipartite lattice which is just a real (or Ising) order parameter. The results achieved should also be useful to Quantum Monte Carlo simulations on the extended boson Hubbard model in a frustrated finite $N = L \times L$ lattice²⁶. The analysis in the direct picture in this section can be contrasted to that by the dual vortex method in the dual picture³⁰.

A. Density-Density and bond-bond correlation functions in a frustrated lattice

In a frustrated lattice, in general, one can write the density at site i as

$$N(\vec{r}_i, t) = n(\vec{r}_i, t) + \text{Re} \sum_{\alpha=1}^P \phi_\alpha e^{i\vec{Q}_\alpha \cdot \vec{r}_i} \quad (58)$$

where $\vec{Q}_\alpha, \alpha = 1, 2, \dots, P$ are the ordering wavevectors, the ϕ_α is the complex CDW order parameter near the \vec{Q}_α . For the X-CDW in Fig.4a, $P = 1$, for the CDW-VBS in Fig.5, $P = 3$. Then the density-density correlation function in Eqn.7 can be written as:

$$\begin{aligned} S_N(\vec{q}, t) = & \frac{1}{N} \sum_i e^{-i\vec{q} \cdot \vec{r}_i} \langle n(i, t) n(0, 0) \rangle_C + n^2 \delta_{\vec{q}, 0} \\ & + \sum_{\alpha=1}^P \left[\frac{1}{N} \sum_i e^{-i(\vec{q} - \vec{Q}_\alpha) \cdot \vec{r}_i} \langle \phi_\alpha(i, t) \phi_\alpha^*(0, 0) \rangle_C \right. \\ & \left. + \frac{1}{N} \sum_i e^{-i(\vec{q} + \vec{Q}_\alpha) \cdot \vec{r}_i} \langle \phi_\alpha^*(i, t) \phi_\alpha(0, 0) \rangle_C \right] \\ & + \sum_{\alpha=1}^P |\langle \phi_\alpha \rangle|^2 (\delta_{\vec{q}, \vec{Q}_\alpha} + \delta_{\vec{q}, -\vec{Q}_\alpha}) \end{aligned} \quad (59)$$

where we have used the translational invariance to get rid of one summation and $\langle n_i(t)n_j(0) \rangle_C = \langle n_i(t)n_j(0) \rangle - n^2$ and $\langle \phi_\alpha^*(i, t)\phi_\alpha(0, 0) \rangle_C = \langle \phi_\alpha^*(i, t)\phi_\alpha(0, 0) \rangle - |\langle \phi_\alpha \rangle|^2$ are connected Green functions. The $\langle \phi_\alpha \rangle = m_\alpha e^{i\theta_\alpha}$ is the expectation value of the CDW order parameter. The translational invariance also dictates $\langle \phi_\alpha^*(i, t)\phi_\beta(0, 0) \rangle = 0$ for $\alpha \neq \beta$.

Its Fourier transform leads to the dynamic structure function:

$$\begin{aligned} S_N(\vec{q}, \omega) &= \int dt e^{-i\omega t} S_N(\vec{q}, t) \\ &= n^2 \delta_{\vec{q}, 0} \delta(\omega) + \sum_{\alpha=1}^P |\langle \phi_\alpha \rangle|^2 (\delta_{\vec{q}, \vec{Q}_\alpha} + \delta_{\vec{q}, -\vec{Q}_\alpha}) \delta(\omega) \\ &+ \frac{1}{N} S_n^{inel}(\vec{q}, \omega) + \frac{1}{N} S_\phi^{inel}(\vec{q}, \omega) \end{aligned} \quad (60)$$

where the first and second $\delta(\omega)$ terms denote the elastic scatterings at $\vec{q} = 0$ and $\vec{q} = \vec{Q}_\alpha$ respectively, the third and the fourth term denote the inelastic scatterings near $\vec{q} = 0$ and $\vec{q} = \vec{Q}_\alpha$ respectively.

From $S_N(\vec{q}, t = 0) = \int \frac{d\omega}{2\pi} S_N(\vec{q}, \omega)$, we can see the equal-time correlation function is the sum of the elastic one and the in-elastic one:

$$S_N(\vec{q}, t = 0) = S_n^{el} + \frac{1}{N} S_n^{inel}(\vec{q}) + S_\phi^{el} + \frac{1}{N} S_\phi^{inel}(\vec{q}) \quad (61)$$

where $S_n^{el} = n^2 \delta_{\vec{q}, 0}$, $S_\phi^{el} = \sum_{\alpha=1}^P |\langle \phi_\alpha \rangle|^2 (\delta_{\vec{q}, \vec{Q}_\alpha} + \delta_{\vec{q}, -\vec{Q}_\alpha})$ and $S_n^{inel}(\vec{q}) = \int \frac{d\omega}{2\pi} S_n^{inel}(\vec{q}, \omega)$, $S_\phi^{inel}(\vec{q}) = \int \frac{d\omega}{2\pi} S_\phi^{inel}(\vec{q}, \omega)$.

In the following, we discuss the density-density correlation functions in the superfluid, CDW and CDW supersolid respectively.

(a) *Superfluid state near the CDW or the CDW-VBS state*

In the superfluid state, the first term in Eqn.59 stands for the gapless superfluid mode near $\vec{q} = 0$ and is also given by Eqn.12. The second term near $\vec{q} = \pm\vec{Q}_\alpha$ in Eqn.59 comes from the roton contribution near $\vec{q} = \pm\vec{Q}_\alpha$ in Fig.10a1. The dispersion near $\vec{q} = \pm\vec{Q}_\alpha$ can be taken as $\omega(\vec{q}) \sim \Delta_{r\alpha} + \frac{(\vec{q} \mp \vec{Q}_\alpha)^2}{2m_{r\alpha}}$ where $\Delta_{r\alpha} > 0$ is the roton gap near $\pm\vec{Q}_\alpha$. There is no CDW order yet, so $\langle \phi_\alpha \rangle = 0$ in the Eqn.59. However, as one approaches the CDW from the SF in Fig.3a, there is a first order transition into the CDW driven by the collapse of all the roton gaps $\Delta_{r\alpha}$.

(b) *CDW or CDW-VBS state*

In the CDW state, the nn correlator near $\vec{q} = 0$ in Eqn.59 is very small, so can be dropped safely, so one only need to focus on the $\phi_\alpha^*\phi_\alpha$ correlator near $\vec{q} = \pm\vec{Q}_\alpha$. The discrete lattice symmetry was broken due to the non-uniform density distribution, so $\langle \phi_\alpha \rangle \neq 0$, there is also a gap $\Delta_{CDW,\alpha}$ in the CDW state, so the connected equal time correlation function decays exponentially in the CDW state: $\langle \phi_\alpha^*(i, 0)\phi_\alpha(j, 0) \rangle_C \sim e^{-|\vec{r}_i - \vec{r}_j|/\xi_{CDW,\alpha}}$ with $\xi_{CDW,\alpha} \sim 1/\Delta_{CDW,\alpha}$, so the in-coherent term in

Eqn.59 is only at the order of $\sim 1/N$, we conclude:

$$\begin{aligned} S_N(\pm\vec{Q}_\alpha, t = 0) &= |\langle \phi_\alpha \rangle|^2 + \frac{1}{N} S_\alpha^{inel}(\vec{q} = \pm\vec{Q}_\alpha) \\ &= |\langle \phi_\alpha \rangle|^2 + O(1/N) \end{aligned} \quad (62)$$

Here we can see that the equal time structure factor is the sum of the elastic scattering $S_\alpha^{el} = |\langle \phi_\alpha \rangle|^2$ plus a $1/N$ in-elastic background.

For $\vec{q} \neq \vec{Q}_\alpha$, but close to \vec{Q}_α , then we find

$$S_N(\vec{q}, t) \sim \frac{1}{N} \sum_i e^{-i(\vec{q} - \vec{Q}_\alpha) \cdot \vec{r}_i} \langle \phi_\alpha(i, t)\phi_\alpha^*(0, 0) \rangle_C \quad (63)$$

where one can extract the excitation spectrum and spectral weight of the CDW near $\vec{q} \neq \pm\vec{Q}_N$ shown in Fig.10c1. Again, the excitation spectrum around $\vec{k} - \vec{Q}_N = \vec{q}$ can also be extracted from the Feynman relation Eqn.17 which holds at $\vec{q} \rightarrow 0$, but not at $\vec{q} = 0$. The f -sum rule $I(\vec{q}) = \int_{-\infty}^{\infty} d\omega \omega S_N(\vec{q}, \omega) = \langle [[n(\vec{q}), H], n(-\vec{q})] \rangle$ also holds independent of the underlying lattices. For example, the Eqn.18 at a $d = 2$ square lattice can be extended to a triangular lattice:

$$\begin{aligned} I(\vec{q}) &= -2t \sum_{\vec{k}} [(\cos q_x - 1) \cos k_x + (\cos q_y - 1) \cos k_y \\ &+ (\cos(q_x + q_y) - 1) \cos(k_x + k_y)] \langle \Psi_0 | b_{\vec{k}}^\dagger b_{\vec{k}} | \Psi_0 \rangle \end{aligned} \quad (64)$$

which can be used to extract the excitation spectra by QMC in both the SF and the CDW state in a triangular lattice. The explicit forms for the f sum rule for other frustrated lattices can be similarly derived.

(c) *CDW Supersolid or CDW-VBS Supersolid state*

In this case, the first term near $\vec{q} = 0$ in Eqn.59 stands for the gapless superfluid mode as given by Eqn.12 and shown in the lower branch in Fig.10b1.

The static order at $\vec{q} = \pm\vec{Q}_\alpha$ is given by Eqn.62 and the dynamic structure factor close to $\pm\vec{Q}_\alpha$ in the upper branch in Fig.10b1 is given by Eqn.63 respectively.

Combining the density-density discussions above in a frustrated lattice with the bond-bond correlation functions in a bipartite lattice presented in Sec.III-B, we can similarly discuss the bond-bond correlation functions in a frustrated lattice

B. Applications to CDW, VBS and CDW-VBS phases in a triangular lattice

From Eqn.2, one can see that the scattering cross section for the X-CDW in 4a is similar to Fig.9a with $\pm\vec{Q}_n = \pm 2\pi/3(1, 1)$ and $\vec{K} = (2\pi, 0)$ as the shortest reciprocal lattice vector of the underlying triangular OL. The CDW order parameter m^2 replaced by $|\langle \phi_c \rangle|^2$ where $\phi_c = A$.

For a triangular lattice, there are three different orientations of bonds aligned along $\hat{a}_1, \hat{a}_d, \hat{a}_2$. From Eqn.3, one can see that Eqn.31 should be generalized to:

$$\hat{K}_\Delta = f_{a_1}(\vec{q}) K_{a_1}(\vec{q}) + f_{a_d}(\vec{q}) K_{a_d}(\vec{q}) + f_{a_2}(\vec{q}) K_{a_2}(\vec{q}) \quad (65)$$

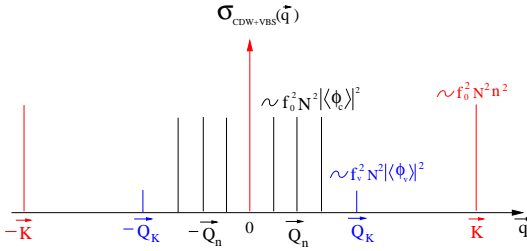


FIG. 12: The characteristics of optical scattering cross section in the CDW+VBS phase in a triangular lattice. The \vec{Q}_n stands for the three CDW ordering wavevectors $\vec{Q}_\alpha = 2\pi/3(1, 0), 2\pi/3(0, 1), 2\pi/3(1, -1), \alpha = 1, 2, 3$. Its magnitude is proportional to the CDW order parameter $|\langle\phi_c\rangle|^2$ in Eqn.62 and Eqn.4. The \vec{Q}_K stands for the extra VBS ordering wavevector $\vec{Q}_4 = 2\pi/3(1, 1)$. Its magnitude is proportional to the VBS order parameter $|\langle\phi_v\rangle|^2$ in Eqn.5. The ratio of the peak at \vec{Q}_n over that at \vec{K} is $\sim |\langle\phi_c\rangle|^2/n^2 \sim 1$, while the ratio of the peak at \vec{Q}_K over that at \vec{K} is $\sim |f_a/f_0|^2|\langle\phi_v\rangle|^2/n^2 \sim 10^{-5}$. It should be visible in the current optical Bragg scattering experiments.

where $\vec{q} = \vec{k}_1 - \vec{k}_0$. For the $\pm\vec{Q}_K = \pm 2\pi/3(1, 1)$ ordering of the Triangular valence bond in Fig.4b, $S_{K1} = S_{Kd} = S_{K2}$ with the VBS order parameter $\phi_{v1} = \phi_{vd} = K_1, \phi_{v2} = K_1 e^{-i2\pi/3}$. So the scattering cross section for the VBS in Fig.4b is similar to Fig.9b with $\pm\vec{Q}_K = \pm 2\pi/3(1, 1)$ and the $\vec{K} = (2\pi, 0)$ as the shortest reciprocal lattice vector of the underlying triangular OL. The VBS order parameter K^2 replaced by $|\langle\phi_v\rangle|^2 = 3K_1^2$.

For the CDW-VBS phase in Fig.5 and Eqn.4, Eqn.5, there are 3 CDW ordering wave vectors $\vec{Q}_\alpha = 2\pi/3(1, 0), 2\pi/3(0, 1), 2\pi/3(1, -1), \alpha = 1, 2, 3$ with the corresponding CDW order parameters $\phi_1 = -\delta e^{i5\pi/18}, \phi_2 = \delta e^{i\pi/18}, \phi_3 = \delta e^{i\pi/18}$. In addition to the same 3 ordering wave vectors, the VBS order has its own new ordering wavevector $\vec{Q}_4 = 2\pi/3(1, 1)$ with the VBS order parameter $\phi_{v1} = \phi_{vd} = c\delta(I_1 + I_2), \phi_{v2} = c\delta(I_1 + I_2)e^{-i2\pi/3}$, so although the scattering cross section $\sim |\langle\phi_c\rangle|^2 \sim \delta^2$ at the ordering vectors $\vec{Q}_\alpha, \alpha = 1, 2, 3$ comes from the sum of the contributions from both the CDW and the VBS, its value $\sim |f_a(\vec{Q}_4)|^2 \times |\langle\phi_v\rangle|^2 \sim |f_a(\vec{Q}_4)|^2 \times c^2\delta^2$ at the ordering wavevector $\vec{Q}_4 = 2\pi/3(1, 1)$ is solely due to the VBS at this ordering wavevector. So the small scattering cross section peak at $\vec{Q}_4 = 2\pi/3(1, 1)$ in Fig.12 can be used to determine the VBS order in the CDW-VBS phase in Fig.5.

The SF to Mott transition in a triangular lattice can be similarly discussed as in Sec.V. The CDW (CDW-VBS) to the CDW-SS (CDW-VB-SS) transition in a triangular lattice can also be similarly discussed as in Sec. VI. However, it was shown in³⁰ that there is no VB-SS in a frustrated lattice, the transition from a VBS to the SF can only be a direct first order, there is no an intervening VB-SS, so the Sect.VII does not apply to a

frustrated lattice.

The generalization to non-Bravais lattices such as the honeycomb, Kagome, Sutherland-Shastry and checkboard lattices^{30,54} can also be worked out similarly.

IX. PHOTON BRAGG SCATTERING EXPERIMENTS

The main difference of light scattering in cold atom systems from that in condensed matter system is that the former is charge neutral, so the off-resonant Raman scattering processes in Fig.6 are involved, what are measured are the density-density and bond-bond correlation functions listed in Eqn.33. While in the latter, the ions carry electric charges, so there is a direct scattering. So the latter usually has a much bigger scattering cross sections. For example, in high T_c superconductors⁴⁷, the ARPES directly measures the single quasi-particle spectral weights.

In the previous sections, we showed that the elastic photon Bragg scattering can not only detect the CDW ordering at $\vec{q} = \vec{Q}_n$ easily (Fig.9a), but also be used to detect the VBS ordering at $\vec{q} = \vec{Q}_K$ (Fig.9b). It is also quite sensitive to the small superfluid component in the CDW-SS and VB-SS. We also showed that the photon Bragg scattering cross section increases from the Mott to the SF phase due to the boson flow through the whole optical lattice inside the SF phase. So this detection method is especially powerful to detect the ground states of various quantum phases. But it may not be easy to detect the excitation spectrum by using this method due to the following reasons: Due to the smallness of the CDW gap $\Delta_{CDW} \sim U \sim 10kHz \sim 1\mu K$ and even smaller VBS gap $\Delta_{VBS} \sim t^2/U \sim nK$ compared to the energy of the incident light $E_i \sim 10^5GHz$, the tiny energy difference $\delta E = E_f - E_i$ is not easy be detected in the present inelastic Bragg scattering experiments. So far, all the previous Bragg scattering experiments⁷ only focused on the elastic scattering with $\omega = 0$ which detect the static orders of OL itself. However, it was argued⁷ that the integrated in-elastic scattering can be used to detect the temperature of cold atoms in OL with incident light intensity $I_{in} \sim 500\mu W/cm^2$ and the detuning in Fig.6 $\Delta \sim 20\gamma$ where γ is the linewidth of the excited state. We expect that the tiny energy difference is still detectable by measuring the quantum beats of phase sensitive homodyne interference experiments. So the possible future combination of the light scattering in Fig.1a combined with the quantum beat measurement can be used to detect not only the ground state, but also the excitation spectrum. Note that in contrast to the atom Bragg spectroscopy to be discussed in the following section, the photon Bragg spectroscopy does not involve the TOF measurements, so it is a non-destructive measurement.

X. ATOM BRAGG SCATTERING EXPERIMENTS

There are also two different Atom Bragg scattering experiments. The Momentum Bragg spectroscopy is more applicable in the superfluid side to detect its Bogoliubov excitations. While the energy Bragg spectroscopy is more applicable in the insulating side to detect its excitation gap. But it may not be as effective as the photon Bragg scattering to detect the ground states of the quantum phases.

(a) Momentum Bragg spectroscopy

It measures the atom diffraction from the light gratings formed by the two laser beams in Fig.1b, so it is a complementary (or dual) to the light scattering which measures the light diffraction from the atoms gratings. It is used to measure the Bogoliubov excitation spectrum inside a superfluid.

The main experimental procedures of the Momentum Bragg spectroscopy⁵ are: (1) The duration of the two incident light pulses in Fig.1b is about $\tau_p \sim 400\mu\text{s}$, then shut off (Fig.13 a). (2) Then the optical lattices and also the trap in Fig.1b are released shortly after the turn-off of the light pulse. (3) Then after some expanding time $\tau_{exp} \sim 200\tau_p \sim 8\text{ms}$, the time of flight images are taken to measure the momentum distribution of the expanding gas. During the expansion process, the energy and momentum of the elementary excitations are transferred to the free particles.

Only when the imparted energy ω and the imparted momentum \vec{k} match the dispersion relation of the elementary excitations in the system, one can observe a scattered cloud (Fig.13 b) whose number $N_{sc}(\vec{q}, \omega)$ is proportional to the dynamic structure factor:

$$N_{sc}(\vec{q}, \omega) \sim \left(\frac{\Omega^2}{\Delta}\right)^2 N^2 [|f_0(\vec{q})|^2 S_n(\vec{q}, \omega) + \sum_{\alpha=\hat{x}, \hat{y}} |f_\alpha(\vec{q})|^2 S_{K_\alpha}(\vec{q}, \omega)] \quad (66)$$

where the prefactor is proportional to the duration τ_p , the incident density $I_{in} \sim 1\text{mW/cm}^2$ in Fig.13. When comparing with Eqn.33, one can see that the scattering cross section in the light scattering experiment is replaced by the scattered clouds in the atom Bragg spectroscopy.

The integrated scattered atoms $N_{sc}(\vec{q}) = \int d\omega N_{sc}(\vec{q}, \omega)$ is proportional to the equal-time response function

$$N_{sc}(\vec{q}) \sim \left(\frac{\Omega^2}{\Delta}\right)^2 N^2 [|f_0(\vec{q})|^2 S_n(\vec{q}) + \sum_{\alpha=\hat{x}, \hat{y}} |f_\alpha(\vec{q})|^2 S_{K_\alpha}(\vec{q})] \quad (67)$$

This can be measured by scanning the frequency ω at fixed \vec{q} . For the current experimental pulse duration time and the incident density, the scattered atoms around $\vec{q} = 0$ are about 10–20% of the condensate atoms around $\vec{q} = 0$:

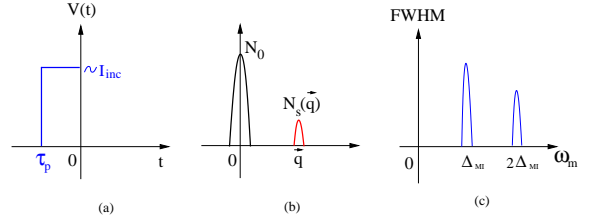


FIG. 13: (a) The duration and strength of the two laser beams in the atom Bragg spectroscopy in Fig.1b. (b) In the momentum transfer Bragg spectroscopy, the scattered atom cloud at \vec{q} versus the condensate cloud at $\vec{q} = 0$. In a TOF image, the momentum is mapped to the axial distance z . So the two peaks are separated by a distance in the axial direction. (c) In the energy Bragg spectroscopy, the full width at half maximum (FWHM) of the central peak in the TOF image peaks when the modulation frequency ω_m matches the Mott gap Δ_{Mott} in the Mott insulating phase. The momentum is fixed at $\vec{q} = 0$ in the Mott state, but can be tuned to \vec{Q}_n or \vec{Q}_K in a CDW or VBS state to measure Δ_{CDW} and Δ_{VBS} respectively.

$N_{sc}(\vec{q})/N_0(\vec{q} = 0) \sim 0.1 - 0.2$. Then one may neglect nonlinear terms at the required laser powers. Possible spontaneous scattering processes can also be suppressed. In real atom Bragg spectroscopy experiments, there are several technical issues such as the signal strength, the geometry dependence, the suppressions of the multi-photon processes and super-radiance... need to be considered, but the basic picture is presented in this section and sketched in the Fig.13.

(b) Energy Bragg spectroscopy

The excitation gaps in the Mott, CDW or VBS and corresponding spectral weights in Fig.10 can be detected by the energy transfer Bragg spectroscopy⁶. In this experiment, the two laser beams in Fig.1b is counter-propagating, so simply super-imposed on the external laser beams forming the optical lattice: $V_{OL}(x, t) = (V_{OL,0}(x, t) + A_m \sin \omega_m t) \cos^2 kx$. The modulation A_m and the frequency difference ω_m introduces two sidebands with frequencies $\pm \omega_m$ relative to the OL laser frequency. So when the imparted energy ω_m matches the excitation gap Δ at $\vec{q} = 0$ or any reciprocal lattice vector \vec{K} inside the Mott state, there is a maximum response of the atoms. After the excitation, the OL potential is ramping down linearly to the SF regime and kept in this shallow potential for some time. Then the trap in Fig.1b is suddenly switched off, the atoms' interference images are taken after their 20ms ballistic expansion. The full width at half maximum (FWHM) of the central peak is taken as the measure of the energy deposited in the atom clouds by the excitation. Namely, the FWHM represents the system's response to the two laser beams in Fig.1b. Indeed, discrete peaks in the FWHM were observed⁶ at discrete spectrum $\omega_m = n\Delta_{MI}$, $n = 0, \pm 1, \dots$ in Fig.13c.

Note that the gaps inside the CDW, VBS, CDW-VBS and the corresponding supersolids in Fig.10 are at mo-

mentum $\vec{q} = \vec{Q}_n$ or $\vec{q} = \vec{Q}_K$. We expect similar energy transfer Bragg spectroscopy can be used to measure these gaps when one tune $\vec{q} = \vec{Q}_n$ or $\vec{q} = \vec{Q}_K$ in Fig.1b and Fig.13c. The corresponding spectral weights are just the areas under the peaks in Fig.13c.

It maybe useful to make a brief comparison between the atom and photon Bragg scattering here, the photon Bragg scattering is very good for detecting the orders, it also does not involve the TOF measurements, so it is a non-destructive measurement. As explained in the previous section, so far, it is very challenging, but still possible to measure the excitation spectrum by using very precise quantum beating interference measurements. However, as discussed in this section, the atom Bragg spectroscopy is not very suitable to detect the ground state orders, especially all the possible insulating states, but very effective to detect the excitation spectra. For example, the superfluid components in the CDW and VBS supersolids can be determined by the momentum⁵ transfer Bragg spectroscopy. The gaps in the CDW and VBS supersolids can be measured by the energy⁶ transfer Bragg spectroscopy. Because the atom Bragg spectroscopy involves the TOF measurements, so it is a destructive measurement. So the photon and atom Bragg spectroscopy are two complementary detection methods, the combinations of both can be used to detect many conventional and exotic quantum phases and their excitation spectra of cold atoms in optical lattices as soon as these phases are within experimental reach.

XI. CAVITY QED DETECTION METHOD

Very recently, a non-destructive method¹⁷ was proposed to detect Mott and superfluid phases by using cavity enhanced off-resonant light scattering from ultra-cold atoms loaded on optical lattices. In the off-resonant scattering, the atom-field detuning Δ is much larger than the atom-field coupling g which, in turn, so the upper level of the atoms can be adiabatically eliminated. However, on the experimental side, the two cavities used in¹⁷ are very hard to implement, on the theory side, all the concepts and calculations on quantum phases and phase transitions in¹⁷ are not correct.

Because the cavity size in the experiment is $L_{cav} 175\mu m$ is so small, it is very difficult to manipulate experimentally the two cavities, so it is necessary to replace the pumping cavity in¹⁷ by a strong classical laser beam in Fig.14a. However, the probing cavity is crucial to enhance the scattered photon mode a along a given direction, then the experiments are much easier to implement. By using this workable experimental set-up, we will develop systematically a theory to detect the nature of quantum phases such as both the ground state and the excitation spectrum above the ground state of interacting bosons loaded in optical lattices. We explicitly show that off-resonant photons not only couple to the density order parameter, but also the valence bond

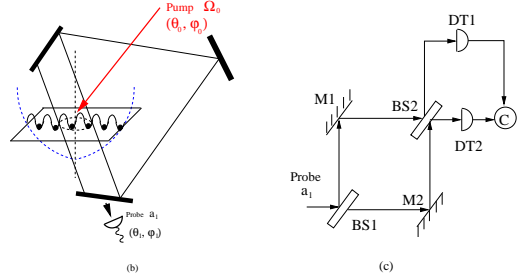


FIG. 14: (a) The classical pump with a Rabi frequency Ω_0 is shined on the 2 dimensional optical lattice at the angle (θ_0, ϕ_0) . A Ring cavity is used to enhance the scattered light a at the angle (θ_1, ϕ_1) . Dashed ellipsis is a trap. Compare with the light scattering experiment Fig.1a. (b) Mach-Zehnder Interferometer⁵³ to detect the single photon correlation function Eqn.75.

order parameter due to the hopping of the bosons on the lattice. By tuning the angles between the classical laser beam and cavity photons, the photon characteristics such as quadrature in Eqn.4 (to be measured by phase sensitive homodyne detection) or one photon correlation functions in Eqn.7 (to be measured by the Mach-Zehnder Interferometer (MZI)) can detect not only the well known superfluid and Mott insulating phases, but also other interesting phases such as charge density wave (CDW), valence bond solid (VBS), CDW supersolid and VBS supersolid.

In the light scattering experiment Fig.1a, the light is scattered to any direction, so one has to use a small aperture to select the light scattered into a given direction \vec{k}_1 . In this section, we propose to replace the aperture by a ring cavity (Fig.14a) to select a cavity photon mode, to enhance the scattered light and also select a given direction \vec{k}_1 . In this section, we will show that by measuring the characteristics of the leaking photon out of the cavity, one can also determine the ground state and excitation spectrum of the atoms loaded in the optical lattice. So the experimental set-up in Fig.14 could be used as alternative to the light scattering experiment in Fig.1a

A non-destructive measurement is to probe the quantum phases formed by two level cold bosons by shining a classical laser beam with a Rabi frequency Ω and with a frequency ω_0 far off the resonant frequency of the two level atoms ω_a and then measure the characteristics of scattered light a from these quantum phases in a cavity with frequency ω_c (Fig.14a). The cavity will greatly enhance the scattering amplitude of the probe photons a . The boson Hamiltonian is given by Eqn.1. Assuming the mode functions $u_l(\vec{r}) = e^{i\vec{k}_l \cdot \vec{r}_i + i\phi_l}$, $l = 0, 1$ for the pump with the frequency ω_0 and the traveling wave with the frequency $\omega_1 = \omega_c$ in a ring cavity (Fig.14b) where the two in-plane momenta of the two lights $\vec{k}_0 = k_0 \sin \theta_0 (\cos \phi_0, \sin \phi_0)$, $\vec{k}_1 = k_1 \sin \theta_1 (\cos \phi_1, \sin \phi_1)$. All the atoms are loaded in optical lattices formed by laser beams with wavevector \vec{k} . The pumping laser beam and

the cavity photon a are much weaker than the standing wave laser beams which form the optical lattices (not shown in Fig.14). When it is far off the resonance, the light-atom detuning $\Delta_{la} = \omega_l - \omega_a$ is much larger than the Rabi frequency Ω_0 which, in turn, is larger than κ and γ , then after adiabatically eliminating the upper level of the two level atoms (Fig.6), in the frame rotating with the pumping frequency ω_0 , the effective cavity QED Hamiltonian describing the interaction among the pumping laser, the off-resonant cavity photons and the ground level is:

$$H_c = (\omega_c - \omega_0)a^\dagger a + \int d^2\vec{x}\Psi^\dagger(\vec{x})[\frac{\Omega_0^2}{\Delta_{0a}} + \frac{g^2}{\Delta_{0a}}a^\dagger a + \frac{g\Omega_0}{\Delta_{0a}}(a^\dagger e^{i(\vec{k}_0 - \vec{k}_1) \cdot \vec{r}} + h.c.)]\Psi(\vec{x}) \quad (68)$$

Again, expanding the ground state atom field operator $\psi_g(\vec{r}) = \sum_i b_i w(\vec{r} - \vec{r}_i)$ in Eqn.28 where $w(\vec{r} - \vec{r}_i)$ is the localized Wannier functions of the lowest Bloch band corresponding to $V_{OL}(\vec{r})$ and b_i is the annihilation operator of an atom at the site i in the Eqn.1, one get:

$$H_c = (\omega_c - \omega_0 + \frac{g^2}{\Delta_{0a}}N_{at})a^\dagger a + \frac{\Omega_0^2}{\Delta_{0a}}N_{at} + \frac{g\Omega_0}{\Delta_{0a}}a^\dagger [\sum_i^K J_{i,i}n_i + \sum_{*}^K J_{i,j}b_i^\dagger b_j] + h.c. \quad (69)*$$

where the interacting matrix element is $J_{i,j} = \int d\vec{r}w(\vec{r} - \vec{r}_i)u_0^*(\vec{r})u_1(\vec{r})w(\vec{r} - \vec{r}_j)$.

It is very instructive to note the similarity and difference between Eqn.69 and Eqn.29. The incident light in Fig.1a and Fig.14 are the same, both are classical lights, but the scattered light is Fig.1a was replaced by the cavity photon a in Fig.14, namely, the classical scattered light is replaced by a quantum photon. So the scattered light Rabi frequency Ω in Eqn.29 is replaced by ga^\dagger in Eqn.69 (very similarly, the scattered light in Fig.6 was replaced by the cavity photon a), the $e^{-i\omega t}$ in Eqn.29 was taken care of by the effective detuning of the cavity photon from the incident light $\Delta_c = \omega_c - \omega_0 + \frac{g^2}{\Delta_{0a}}N_{at}$ in Eqn.69. In view of these similarity and differences, the $\hat{D} = \sum_i^K J_{i,i}n_i$ and $\hat{K} = \sum_{*}^K J_{i,j}b_i^\dagger b_j*$ in Eqn.69 can be very similarly manipulated as in Eqn.30 and 31 respectively.

In this section, we focus on the global illumination $K = N$ in Fig.14a. If there is a wedding cake structure inside a trap¹ (see also appendix B), then $K = N_P$ is the number of atoms in a given phase P in the wedding cake. This can be more easily realized inside a flat trap⁴² or inside a harmonic trap with only one shell structure such as in Fig.15.

It is constructive to compare with the photon-exciton coupling $i\sum_k g(k)a_k^\dagger b_{\vec{k}} + h.c.$ in the electron-hole bilayer (EHBL) system⁵⁰⁻⁵² where photons couple to the SF order parameter $b_{\vec{k}}$ directly. Here the photons couple to both the density order parameter and also the valence

bond order parameter instead of coupling to the SF order parameter directly. However, as shown in Eqn.12, inside the SF state, the density-density correlation function can also reflect the nature of SF precisely. So the coupling in Eqn.69 can reflect all the three orders: density order, valence bond order and SF order precisely.

The Heisenberg equation of motion for a is:

$$\frac{da}{dt} = -i\Delta_c a - i\frac{\Omega_0 g}{\Delta_{0a}}(\hat{D} + \hat{K}) - \kappa a + F(t) \quad (70)$$

where $\Delta_c = \omega_c - \omega_0 + \frac{g^2}{\Delta_{0a}}N_{at}$ stands for the effective detuning to the pumping frequency. The $F(t)$ is the noise operator satisfying: $\langle F^\dagger(t)F(t') \rangle = \kappa \bar{n}_{\omega_c} \delta(t - t')$, $\langle F(t)F^\dagger(t') \rangle = \kappa(\bar{n}_{\omega_c} + 1)\delta(t - t')$, $\langle F(t)F(t') \rangle = \langle F^\dagger(t)F^\dagger(t') \rangle = 0$ where $\bar{n}_{\omega_c} = 1/(e^{\omega_c/T} - 1)$ and T is the temperature of the reservoir.

(a) *One time average: photon expectation value*

The stationary solution for the Heisenberg equation of motion for a Eqn.70 is:

$$\langle a \rangle = CN(\langle \hat{D} \rangle + \langle \hat{K} \rangle) \quad (71)$$

$$\text{where } C = -\frac{i\Omega_0 g}{\Delta_{0a}(\kappa - i\Delta_c)}.$$

Substituting Eqn.30 and 31 into the Eqn.71 leads to

$$\langle a(\vec{q}) \rangle = CN(\langle n(\vec{q}) \rangle + f_x(\vec{q})\langle K_x(\vec{q}) \rangle + f_y(\vec{q})\langle K_y(\vec{q}) \rangle) \quad (72)$$

which can be measured by phase sensitive homodyne measurement^{51,53}.

Again, we first look at the SF to Mott transition at integer fillings as discussed in Sect.V. Inside the SF, the $K_{i,i+\hat{x}} = K_{i,i+\hat{y}}$ is uniform which depends on $t - t_c$ in Fig.8, so at a reciprocal lattice $\vec{q} = \vec{K}$, Eqn.72 leads to:

$$\langle a(\vec{q}) \rangle_{SF} - \langle a_1(\vec{q}) \rangle_{Mott} = 2CNf_x(\vec{q})K \quad (73)$$

which can be detected by phase sensitive homodyne detection^{51,53}. It is an effective measurement of the kinetic energy inside the SF. This measurement can be contrasted to the increase of the scattering cross section from the Mott to the SF shown in Eqn.37 or from the CDW to CDW-SS, or from the VBS to VB-SS discussed in Section VI-a and VII-a respectively.

(b) *Two time averages: single photon correlation functions*

Now we need to calculate the two-time one photon correlation function. The solution of Eqn.70 is:

$$a(t) = e^{-(\kappa + i\Delta_c)(t - t_0)}a(t_0) + \int_{t_0}^t d\tau e^{-(\kappa + i\Delta_c)(t - \tau)}(\eta_a(\tau) + F(\tau)) \quad (74)$$

where $\eta_a(t) = -i\frac{\Omega_0 g}{\Delta_{0a}}(\hat{D}(t) + \hat{K}(t))$ stands for the "effective" pumping force on a from the atoms.

We observe the following three important facts: (1) If $t - t_0 \gg 1/\kappa$, the first term drops out. (2) The second term contributes significantly only when $t - \tau < 1/\kappa$.

It was known that in an optical lattice^{3,4}, the hopping energy scale is much smaller than the cavity decay energy scale: $J \sim 10^3 \text{Hz} \ll \kappa \sim 10^7 \text{Hz}$, so we can approximate $\eta_a(\tau) \sim \eta_a(t)$ when $t - \tau < 1/\kappa$. (3) In the cavity optical frequency regime $\hbar\omega_c \gg k_B T$, so $\bar{n}(\omega_c) \sim 0$, then the noise term drops out for a normal ordered correlation functions. The three facts lead to the two time photon correlation function:

$$\begin{aligned} \langle a^\dagger(\vec{q}, t)a(\vec{q}, 0) \rangle &= |C|^2[\langle D^*(\vec{q}, t)D(\vec{q}, 0) \rangle \\ &+ \langle K^*(\vec{q}, t)K(\vec{q}, 0) \rangle] \end{aligned} \quad (75)$$

where $\vec{q} = \vec{k}_1 - \vec{k}_0$. We expect the crossing correlator $\langle D^*(\vec{q}, t)K(\vec{q}, 0) \rangle$ is negligibly small in any phases. As shown in the Fig.14b, using the Mach-Zehnder Interferometer (MZI)⁵³ and adjusting the difference between the two light paths, one can measure this two time one photon correlation function.

From Eqn.75, one can see that at any given momentum \vec{q} , the Fluorescence spectrum of the probing photons $I(\vec{q}, \omega) = \int d\tau e^{-i\omega\tau} \langle a^\dagger(\vec{q}, t + \tau)a(\vec{q}, t) \rangle$ is :

$$\begin{aligned} I(\vec{q}, \omega) &= |C|^2 N^2 [|f_0(\vec{q})|^2 S_n(\vec{q}, \omega) \\ &+ \sum_{\alpha=\hat{x}, \hat{y}} |f_\alpha(\vec{q})|^2 S_{K_\alpha}(\vec{q}, \omega)] \end{aligned} \quad (76)$$

which is similar to Eqn.33 or Eqn.66 after replacing $(\frac{\Omega^2}{\Delta})^2$ by $|C|^2$.

In Eqn.75, by setting $t = 0$, one can see that the leaking photon number gives precisely the structure factor:

$$\begin{aligned} n_{ph}(\vec{q}) = \langle a^\dagger(\vec{q})a(\vec{q}) \rangle &= |C|^2 N^2 [|f_0(\vec{q})|^2 S_n(\vec{q}) \\ &+ \sum_{\alpha=\hat{x}, \hat{y}} |f_\alpha(\vec{q})|^2 S_{K_\alpha}(\vec{q})] \end{aligned} \quad (77)$$

which is similar to Eqn.35 or Eqn.67 after replacing $(\frac{\Omega^2}{\Delta})^2$ by $|C|^2$. All the discussions in previous sections can also be applied here. For example, the scattering cross sections in a square lattice Fig.9 or in a triangular lattice Fig.12 should just be replaced by the photon numbers at the corresponding wavevectors. So we show that the Fluorescence spectrum of the leaking cavity photons can directly reflect the ground state and the excitation spectrum of any quantum state.

XII. CONCLUSIONS

Due to the dilutees and charge neutral of cold atoms, the experimental ways to detect possible quantum phases and quantum phase transitions of cold atoms in optical lattices in a minimum destructive way remain very limited. In this paper, we developed a systematic and unified theory to use the three different experiments: optical Bragg scattering, atom Bragg spectroscopy or off-resonant cavity enhanced scattering to detect the ground states, the elementary excitation spectra and the corresponding spectral weights of many quantum phases in

both bipartite and frustrated lattices. We show that the two photon Raman processes in all the three measurements not only couple to the density order parameter, but also the valence bond order parameter due to the hopping of the bosons on the lattice. This coupling to the VBS order is extremely sensitive to the superfluid order or VBS order at corresponding ordering wavevectors. It is this coupling which make the three experiments being able to detect not only the well known SF and Mott phases, but also many other important phases such as CDW, VBS, CDW-VBS and all kinds of supersolids. The first experiment^{5,6} was well established, the second^{9,10} is being performed in several experimental groups, the third is a possible new experimental set-up complementary to the first two. The combinations of the three can be used as powerful and complete tools to study the properties of many quantum phases of atoms in optical lattices.

From symmetry points of view, we analyzed several general properties of the density-density and bond-bond correlation functions in both bipartite and frustrated lattices. The CDW and VBS order parameters in bipartite lattices are Ising order parameter m and K respectively, while those in frustrated lattices are complex $U(1)$ order parameter ϕ_c and ϕ_v respectively. This difference leads to several new features of light scattering cross section in frustrated lattices. Previous literatures in quantum phase transitions focused on computing order parameter correlation functions. Here, motivated by the fact that all the three experimental inelastic scattering only couples to the density-density correlation function instead of coupling to the order parameter directly, we computed the density-density correlation function in the Mott phase, Superfluid phase and the quantum critical regime in both $z = 1$ and the $z = 2$ universality class in Fig.8 and Fig.11 respectively.

At integer fillings, when \vec{q} matches a reciprocal lattice vector \vec{K} of the underlying OL, there is a increase in the optical scattering cross section as the system evolves from the Mott to the SF state. This increase may be used as an effective measure of the average kinetic energy inside the SF. At half integer fillings, in the CDW state, when \vec{q} matches the CDW ordering wavevector \vec{Q}_n and \vec{K} , there is a diffraction peak proportional to the CDW order parameter squared and the density squared respectively (Fig.9a), the ratio of the two peaks are good measure of the CDW order parameter. In the VBS state, when \vec{q} matches the VBS ordering wavevector \vec{Q}_K , there is a much smaller, but detectable diffraction peak proportional to the VBS order parameter squared, when it matches \vec{K} , there is also a diffraction peak proportional to the uniform density in the VBS state (Fig.9b). The ratio of the two peaks are good measure of the VBS order parameter. All the diffraction peaks scale as the square of the numbers of atoms inside the trap. All these characteristics can determine uniquely CDW and VBS state at commensurate fillings and the corresponding CDW supersolid and VBS supersolid slightly away from the commensurate fillings. In a frustrated lattice such as a

triangular lattice, there are a new kind phase with both CDW and VBS orders called CDW+VBS phase in Fig.5. There are corresponding several new features in the light scattering cross sections. We also describe how it can detect both the CDW order $|\langle\phi_c\rangle|^2$ and the VBS order $|\langle\phi_v\rangle|^2$ in the CDW-VBS phase in Fig.12. We also point out that due to the smallness of the CDW gap and even smaller VBS gap compared to the energy of the incident light, the tiny energy difference $\delta E = E_f - E_i$ could be detected by quantum beats in phase sensitive homodyne interference experiments. The superfluid components in the CDW and VBS supersolids can be determined by the momentum⁵ transfer Bragg spectroscopy. While the excitation gaps in the CDW and VBS and corresponding spectral weights can be detected by the energy transfer⁶ Bragg spectroscopy. So the combinations of these photon and atom scatterings can be used to detect many conventional and exotic quantum phases and their excitation spectra of cold atoms in optical lattices as soon as these phases are within experimental reach.

We also propose the cavity QED as another possible effective detection method. It is constructive to compare Fig.14 with the very recent experiments to realize the Z_2 super-radiant phase¹⁹ and to realize all kinds of bi-stabilities in BEC, BEC spinor, fermion or spin-orbit coupled systems¹³⁻¹⁶. In the super-radiant experiment¹⁹, the pumping is a transverse pumping similar to that in Fig.14. The system is in a good cavity limit, so the Hamiltonian dynamics dominates over any dissipation process. As the transverse pumping power increases above a critical value, the system will evolve from a normal phase into a super-radiant phase. So the pumping laser is used to induce the dramatic change of the ground state through the Raman transition. The change of the ground state and the collective excitation spectrum of the strongly coupled atom-photon system can be detected by the fluorescence spectrum. In the bi-stability experiments¹³⁻¹⁶, the pumping is a longitudinal pumping, so it pumps the cavity photon directly, no Raman process in Fig.6 is involved. As the longitudinal pumping power increases above a critical value, the system will suffer bi-instabilities, even tri-instabilities¹⁶. So the pumping laser is also used to change the properties of the strongly coupled photon-atom system by non-linear effects which can be detected by cavity transmission spectrum. The system is in a bad cavity limit. In both cases, the pumping is strong which induces highly non-linear optical and matter effects. The approximation is a two level matter wave approximation which is justified in the strong pumping case. However, in the present cavity QED detection scheme in Fig. 14, the classical laser is used to just probe the quantum phases of the cold atoms so that it will not disturb the properties of the system itself. The cavity is in the bad cavity limit. The approximation we made is a linear response theory which is justified in the weak pumping regime. But we treat all the matter modes exactly which are what one like to detect by the fluorescence spectrum. Furthermore, the cavity QED detection

does not involve the TOF measurements, so it is non-destructive. However, putting OL inside a ring cavity shown in Fig. 14 may still present serious experimental challenges.

Acknowledgements

We thank G.G. Batrouni, I. Bloch, Jason Ho, R. Hulet, S. V. Isakov, Jeff Oh, Juan Pino, R. Scalettar and Han Pu for very helpful discussions. J. Ye also thanks Jason Ho, A. V. Balatsky and Han Pu for their hospitalities during his visit at Ohio state university, the LANL and Rice university where part of this work is done. J. Ye's research is supported by NSF-DMR-0966413, NSFC-11074173, at KITP is supported in part by the NSF under grant No. PHY-0551164. Y. Chen's research was supported by the National Natural Science Foundation of China (Grant No. 10874032), the State Key Programs of China (Grant no. 2009CB929204) and Shanghai Municipal Government. W.M. Liu's research was supported by NSFC-10874235. W.P. Zhang's research was supported by the National Basic Research Program of China (973 Program) under Grant No.2011CB921604, and NSFC under Grant Nos.10588402 and 10474055.

Appendix A: Superfluid stiffness and QED detection at the classical diffraction minima

$$\vec{q} = (\pi, \pi).$$

The Cavity QED scattering from the SF and Mott phase at 1d was addressed in¹⁷. Particularly, they discussed the cavity QED scattering from the Mott and the SF phase at the geometry to suppress the classical diffraction. In this geometry, $\theta_0 = 0, \theta_1 = \pi/2$ in Fig.14a, so $\hat{D} = \sum_i (-1)^i n_i$, so $\langle a_1^\dagger a_1 \rangle_{MI} = 0$ in the $t/U \rightarrow 0$ limit in Fig.8 (see below Eqn.A3). In Ref.¹⁷, the SF ground state was taken as a non-interacting BEC state $|BEC\rangle_{non} \sim (\sum_i b_i^\dagger)^N |0\rangle$. the results in¹⁷ on the SF side are based on the fact that the non-local pair correlation functions between the atom numbers at different sites $\langle n_i n_j \rangle$ in the non-interacting BEC state are the same for any $i \neq j$. This infinite long-range correlation is certainly not valid in any SF, so their photon spectrum on the SF side are in-correct. In this appendix, we will calculate the photon number spectrum inside the SF phase and show that it is an effective measure of the superfluid density ρ_s and the phonon velocity v of the SF. While the two fundamental physical quantities for the SF are not even defined for the non-interacting BEC state.

It is well known that a non-interacting BEC state is a pathological state. A repulsive interaction is needed to transform the BEC state to a SF state and leads to the gapless Goldstone mode above the SF ground state shown in Eqn.12 and in Fig.10. The Fourier transform of the equal density-density correlation function in Eqn.13 at $d = 2$ is:

$$\langle \delta n_i \delta n_j \rangle_{SF} = \langle n_i n_j \rangle - n^2 \sim \rho_s / v |i - j|^3 \quad (A1)$$

which decays as a power law as the distance between the

two sites $|i - j| \gg a$ due to the gapless Goldstone mode in the SF and also depends on the superfluid density ρ_s and the Goldstone mode velocity v . Strictly speaking, Eqn.A1 only holds at very long distance $|i - j| \gg a$, for example, it certainly breaks down at $i = j$, but we expect $\langle n_i^2 \rangle_{SF} - n^2 \sim \rho_s/v$ still holds. In contrast, from Eqn.14, inside the Mott state

$$\langle \delta n_i \delta n_j \rangle_{MI} = \langle n_i n_j \rangle - n^2 \sim e^{-|i-j|/\xi_{MI}} \quad (A2)$$

where $\xi_{MI} \sim 1/\Delta_{MI}$ is the correlation length inside the Mott state. This equation is consistent with Eqn.40 in the momentum space in the Mott phase.

While at the QCP between the SF to Mott transition in Fig.8, because δn is a conserved quantity, so no anomalous dimension, then we have:

$$\langle \delta n_i \delta n_j \rangle_{QC} = \langle n_i n_j \rangle - n^2 \sim 1/|i - j|^4 \quad (A3)$$

for $|i - j| \gg a$. This equation is consistent with Eqn.43 in the momentum space at the QC.

Then from Eqn.75, we can see that at $\vec{q} = (\pi, \pi)$, the photon number is $\langle a^\dagger(\vec{q}, 0) a(\vec{q}, 0) \rangle = |C|^2 \langle D^*(\vec{q}, 0) D(\vec{q}, 0) \rangle = |C|^2 \sum_{i,j} (-1)^{i-j} \langle n_i n_j \rangle = |C|^2 N \sum_j (-1)^{i-j} [\langle n_i n_j \rangle - n^2]$. By using Eqn.A1 and Eqn.A2, we can see that $\langle a^\dagger(\vec{q}, 0) a(\vec{q}, 0) \rangle_{SF} \sim |C|^2 N \rho_s/v$ and $\langle a^\dagger(\vec{q}, 0) a(\vec{q}, 0) \rangle_{MI} \sim 0$ in the $t/U \rightarrow 0$ limit in Fig.8. So the photon number at $\vec{q} = (\pi, \pi)$ maybe an effective measurement of the superfluid density ρ_s inside the SF. The same conclusions apply to the light scattering cross section after replacing $|C|^2$ by $(\frac{\Omega^2}{\Delta})^2$.

Appendix B: Possibility to observe a supersolid in a shell structure inside a trap.

It is well known that due to the harmonic trap, the local chemical potential will decrease from the center of the trap to the boundary, so there are always a shell structure of phases inside a trap instead of a pure phase. For example, at filling $n = 1$, there is a Mott phase at the center, then there is always a SF shell around the boundary (Fig.15).

It remains challenging to observe a stabilized supersolid in a cold atom experiment, the shell structure inside a harmonic trap may be helpful to make the observation possible. For hard core bosons, it was shown by the QMC in²³, the $(\pi, 0)$ stripe SS may be stable. Now if we take a half filling at the center of the trap, so it is a CDW at the center, a SF near the boundary, then it may be interesting to see if there is a stable vacancy-like CDW-supersolid^{29,30} separating the CDW from the SF (Fig.16). This is a ring structure with a periodic boundary condition around the center, so it may be favorable to stabilize this SS in the quasi-1d ring structure. Indeed, a SS was found to be stable in 1d optical lattice in²⁵.

For soft core bosons, it was shown by the QMC in a square lattice²⁴ and a honeycomb lattice³¹, there is

a always a (π, π) SS sandwiched between the CDW-II

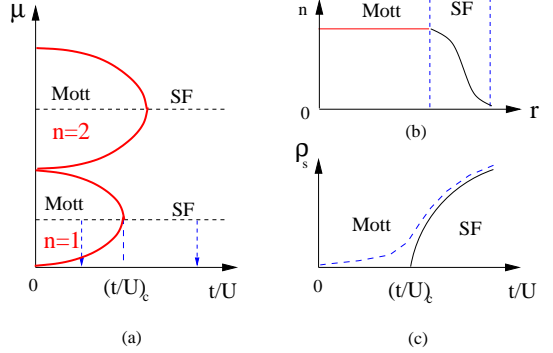


FIG. 15: (a) The zero temperature phase diagram of a homogeneous short-ranged boson Hubbard model³. See Fig.8 for its finite temperature phase diagram. Comparing with the long-range case in Fig.3 and Fig.16. Inside a trap, the local chemical potential $\mu(r) = \mu - \frac{1}{2} \alpha r^2$ decreases from the center to the boundary. (b) The well-known shell structure of Mott state in the center and the SF in the boundary (c) The red solid line is the superfluid density in a homogeneous system with $\rho_s \sim (t - t_c)^\nu$. The blue dashed line is inside a trap

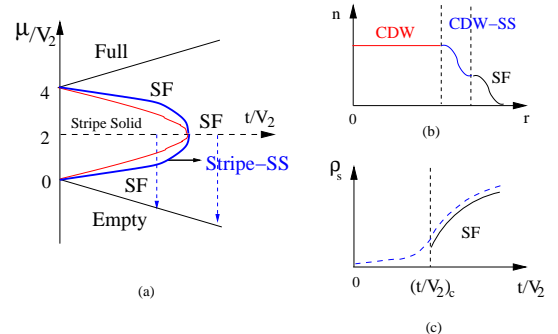


FIG. 16: (a) The zero temperature phase diagram of a homogeneous long-range boson Hubbard model²³. Comparing with the Fig.3. (b) The shell structure of CDW (here is a stripe) state in the center and the SF in the boundary with the CDW-SS intervening between the two (c) The red solid line is the superfluid density in a homogeneous system with ρ_s jump continuously at the CDW-SF transition. The blue dashed line is inside a trap

where the total filling factor is 1 and the CDW-I where the total filling factor is 1/2. In the experiments with dipolar bosons³⁸, if we take an integer filling at the center of the trap, so it is in a CDW-II at the center, then a CDW-I in the middle, a SF near the boundary, then it may be interesting to see if there is a stable ring structure interstitial-like CDW-SS separating the CDW-II from the CDW-I. Although the QMC in^{24,31} shows that there is always a phase separation between the CDW-I and the SF in a flat lattice, it is still possible that there is a ring structure vacancy-like CDW-SS intervening between the CDW-I and the SF. A future extensive QMC inside a harmonic trap is needed to answer all these questions.

¹ For a review, see M. Lewenstein, *et al*, *Adv. Phys.* 56, 243-379 (2007). I. Bloch, J. Dalibard, W. Zwerger, *Rev. Mod. Phys.* 80, 885 (2008).

² Fisher M. P. A., Weichman P. B., Grinstein G. and Fisher D. S., *Phys. Rev. B* 40, 546 (1989).

³ D. Jaksch, C. Bruder, J. I. Cirac, C. W. Gardiner, and P. Zoller, *Phys. Rev. Lett.* 81, 3108 - 3111 (1998).

⁴ M. Greiner, *et al*, *Nature* 415, 39-44 (2002).

⁵ M. Kozuma, *et.al*, *Phys. Rev. Lett.* 82, 871 (1999); J. Stenger, *et al*, *Phys. Rev. Lett.* 82, 4569 (1999); D. M. Stamper-Kurn *et al*, *Phys. Rev. Lett.* 83, 2876 - 2879 (1999); J. Steinhauer, *et.al*, *Phys. Rev. Lett.* 88, 120407, (2002); S. B. Papp, *et.al*, *Phys. Rev. Lett.* 101, 135301 (2008); P. T. Ernst, *et al*, *Nature Physics* 6, 56 (2010).

⁶ T. Stoferle *et al*, *Phys. Rev. Lett.* 92, 130403 (2004).

⁷ G. Birk, *et al*, *Phys. Rev. Lett.* 75, 2823 (1995); M. Weidmller, *et al*, *Phys. Rev. Lett.* 75, 4583 (1995), *Phys. Rev. A* 58, 4647 (1998).

⁸ J. Ruostekoski, C. J. Foot, and A. B. Deb, *Phys. Rev. Lett.* 103, 170404 (2009).

⁹ T. A. Corcovilos *et al*, *Phys. Rev. A* 81, 013415 (2010).

¹⁰ I. Bloch, private communication.

¹¹ F. Brennecke, *et. al* *Nature* 450, 268 (2007).

¹² Yves Colombe, *et al* *Nature* 450, 272 (2007).

¹³ F. Brennecke, S. Ritter, T. Donner, T. Esslinger, *SCIENCE VOL 322 10 OCTOBER 2008 235.*

¹⁴ Lu Zhou, *et.al*, *Phys. Rev. Lett.* 103, 160403 (2009).

¹⁵ R. Kanamoto and P. Meystre, *Phys. Rev. Lett.* 104, 063601 (2010).

¹⁶ Ying Dong, Jinwu Ye and Han Pu, *Phys. Rev. A* 83, 031608 (R) (2011).

¹⁷ I. B. Mekhov, C. Maschler, and H. Ritsch, *Phys. Rev. Lett.* 98, 100402 (2007); *Phys. Rev. A* 76, 053618 (2007); *Nature Physics* 3, 319 - 323 (01 May 2007).

¹⁸ W. Chen, D. Meiser, and P. Meystre, *Phys. Rev. A* 75, 023812 (2007).

¹⁹ K. Baumann, *et.al*, *Nature* 464, 1301-1306 (2010).

²⁰ A. T. Black, H. W. Chan and V. Vuletic, *Phys. Rev. Lett.* 91, 203001(2003).

²¹ Jinwu Ye and CunLin Zhang, *arXiv:0912.1982*, Updated version submitted to *Phys. Rev. lett.*

²² G. Murthy, D. Arovas, A. Auerbach , *Phys. Rev. B* 55, 3104-3121 (1997).

²³ F. Hebert *et.al*, *Phys. Rev. B* 65, 014513 (2001)

²⁴ P. Sengupta, *et.al*, *Phys. Rev. Lett.* 94, 207202 (2005).

²⁵ G.G. Batrouni, *et.al* *Phys. Rev. Lett.* 97, 087209 (2006), *Phys Rev A72, 031601(R)* (2005).

²⁶ S. V. Isakov, *et al*, *Phys. Rev. Lett.* 97, 147202 (2006); Kedar Damle, T. Senthil, *Phys. Rev. Lett.* 97, 067202 (2006).

²⁷ Balents L, *et al*, *Phy. Rev. B* 71, 144508 (2005).

²⁸ Longhua Jiang and Jinwu Ye, *J. Phys, Condensed Matter*. 18 (2006) 6907-6922

²⁹ Jinwu Ye, *cond-mat/0503113*, *Nucl. Phys. B* 805 (3) 418-440 (2008).

³⁰ Yan Chen and Jinwu Ye, *arXiv:0804.3429 v3* and *cond-mat/0612009 v4*.

³¹ Jing Yu Gan, *et. al* , *Phys. Rev. B* 75, 214509 (2007).

³² The CDW and VBS gaps are within the lowest Bloch band, so the approximation of neglecting the higher Bloch bands is justified.

³³ This is similar to non-collinear order (or spiral order) in a frustrated Anti-ferromagnet where the order parameter can be written as $\vec{S}(\vec{r}) = \vec{n}_1 \cos \vec{Q} \cdot \vec{r} + \vec{n}_2 \sin \vec{Q} \cdot \vec{r} = (\vec{n}_1 - i\vec{n}_2)e^{i\vec{Q} \cdot \vec{r}} + h.c.$ where $\vec{n}_1^2 = \vec{n}_2^2 = 1, \vec{n}_1 \cdot \vec{n}_2 = 0$.

³⁴ G. Grynberg, B. Lounis, P. Verkerk, J.-Y. Courtois, and C. Salomon, *Phys. Rev. Lett.* 70, 2249 - 2252 (1993).

³⁵ L. Santos, M. A. Baranov, J. I. Cirac, H.-U. Everts , H. Fehrmann1, and M. Lewenstein, *Phys. Rev. Lett.* 93, 030601 (2004). B. Damski, H. Fehrmann, H.-U. Everts, M. Baranov, L. Santos, and M. Lewenstein1, *Phys. Rev. A* 72, 053612 (2005).

³⁶ A. Griesmaier, *et.al*, *Phys. Rev. Lett.* 94, 160401 (2005)

³⁷ K.-K. Ni, *et al*, *Science* 322, 231 (2008).

³⁸ B. Capogrosso-Sansone, *et al*, *arXiv:0906.2009*.

³⁹ G. Pupillo, *et al*, *arXiv:1001.0519*.

⁴⁰ H. P. Bchler, *et.al*, *Phys. Rev. Lett.* 95, 040402 (2005).

⁴¹ Jinwu Ye, Wuming Liu, Keye Zhang, Yan Li, Weiping Zhang, *Phys. Rev. A* 83, 051604 (R) (2011).

⁴² T.P. Meyrath, *et.al*, *Phys. Rev. A* 71, 041604 (2005).

⁴³ Jinwu Ye, *Phys. Rev. Lett.* 97, 125302 (2006); *Europhysics Letters*, 82 (2008) 16001; *J. Low Temp Phys*, 160, 71 (2010).

⁴⁴ Jinwu Ye and Longhua Jiang, *Phys. Rev. Lett.* 98, 236802 (2007); Jinwu Ye, *Phys. Rev. Lett.* 97, 236803 (2006), *Annals of Physics*, 323, 580-630, (2008); *J. Low Temp. Phys.* 158, 882, (2010).

⁴⁵ A. Chubukov, S. Sachdev and Jinwu Ye, *Phys.Rev.B*, 11919 (1994). Note that the large N expansion in this paper did not apply to the XY case here with $N = 2$ due to the spatial topological vortices at $d = 2, N = 2$.

⁴⁶ Subir Sachdev, T. Senthil, and R. Shankar, *Phys. Rev. B* 50, 258 (1994);

⁴⁷ Jinwu Ye, *Phys. Rev. Lett.* 87, 227003 (2001); *Phys. Rev. B*. 65, 214505 (2002).

⁴⁸ O.I. Motrunich and A. Vishwanath, *Phys. Rev. B* 70, 075104 (2004); T. Senthil, Ashvin Vishwanath, Leon Balents, Subir Sachdev, M. P. A. Fisher, *Science* 303, 1490 (2004); *cond-mat/0312617*.

⁴⁹ For example, see L. H. Ryder, *Quantum Field Theoy*, Cambridge University Press, 2001.

⁵⁰ Jinwu Ye, T. Shi and Longhua Jiang, *Phys. Rev. Lett.* 103, 177401 (2009).

⁵¹ T. Shi, Longhua Jiang and Jinwu Ye, *Phys. Rev. B* 81, 235402 (2010).

⁵² Jinwu Ye, T. Shi, Longhua Jiang, Yinchen He and Yan Chen, *arXiv:0802.1065. V4*. updated version to be submitted to *Phys. Rev.B*.

⁵³ M. O. Scully and M. S. Zubairy, *Quantum Optics*, Cambridge University press, 1997

⁵⁴ For a review, see C. Lhuillier and G. Misguich, *arXiv:cond-mat/0109146*.